Deng et al. *Quantum Frontiers* (2025) 4:4
https://doi.org/10.1007/s44214-025-00077-5

Quantum Frontiers

ORIGINAL ARTICLE Open Access

# Proposal for the high-dimensional quantum computation in ladder-shaped atomic tweezer arrays

Xing Deng[1,2†], Guangshan Peng[1†], Di Xiang[3†], Xiao-fan Xu[1*], Lushuai Cao[1*] and Zhong-Kun Hu[1*]

**Abstract**

Neutral atomic tweezer arrays have become a promising platform for quantum computation, which possess rich degrees of freedom (DoFs) as an important resource for encoding quantum information. We explore the DoF quantum resource in a ladder-shaped atomic tweezer array and propose a scheme of high-dimensional universal quantum computation. This scheme encodes qubits to two degrees of freedom of a single atom, namely the motional (Mo) and the site-occupation (SO) DoFs, which allows one atom to carry two qubits and results in a two-layer qubit architecture. The single-qubit rotational gates on Mo- and SO-qubits, as well as the intra- and inter-DoF Controlled-NOT (CNOT) gates are designed, and the crosstalk between qubits encoded with different DoFs is particularly addressed and compensated by the strategy composed of the detuning engineering and multi-chromatic Hamiltonian modulation. Quantum circuits are assembled from these gates in the ladder-shaped atomic array, generating the hyper and hyper-hybrid entangled states between the Mo and SO DoFs. Our work paves the way for high-dimensional quantum computation with multiple DoFs.

**Keywords:** Ladder-shaped tweezer array, High-dimensional universal quantum computation, Multiple degrees of freedom, Two-layer qubit architecture

## 1 Introduction

The rapid development of the manipulation technologies on the neutral atom array has made this setup a versatile platform for quantum information processing. It has been experimentally realized the individual control and detection of ultracold atoms in a single tweezer [1–5], engineering interactions via the Rydberg excitation [6–10], and the configuration of two [9, 11–13] and three dimensions [14, 15] neutral atomic arrays. These operations benefit the parallel implementation of high-fidelity multi-qubit gates [16, 17], the construction of programmable large-scale quantum simulator [3, 18–20], and the coherent transport of entangled atom arrays [21], which enables the atomic tweezer array as a promising physical platform for realizing large scalable programmable quantum computation, quantum simulation, and quantum sensing [4, 16, 22–24].

Besides the flexible controllability, the multiple degrees of freedom of atoms confined in the tweezer array have also drawn growing attention, and the spin, motional (Mo), and site-occupation (SO) degrees of freedom (DoFs) have been recognized as an important quantum resource. For instance, the Mo states in a single tweezer can be mapped to the SO states among different tweezers, allowing the manipulation and detection of the Mo states [5]. Moreover, the Mo DoF has been exploited to generate a two-atom entangled state in a single tweezer [25], which is then transferred to the spin DoF for spatial transport of the entan-

*Correspondence: xiaofanxu@live.com; lushuai_cao@hust.edu.cn; zkhu@hust.edu.cn
[1] MOE Key Laboratory of Fundamental Physical Quantities Measurement, Hubei Key Laboratory of Gravitation and Quantum Physics, PGMF, and School of Physics, Huazhong University of Science and Technology, Wuhan 430074, People's Republic of China
Full list of author information is available at the end of the article †Equal contributors

glement. There have also been attempts to explore the SO DoF for quantum computation and combine both the spin and the SO DoFs to realize the simultaneous mapping of the charge and gauge sector of the gauge theory [26]. More recently the hyper-entanglement between the spin and Mo DoFs of tweezer atoms has been experimentally generated [27]. These works have witnessed a trend to explore the DoF resource and integrate different DoFs on a single platform to enhance the performance of the atomic tweezer array for quantum computation tasks.

In this work, we propose a scheme to integrate the Mo states in single tweezers and the SO states among different tweezers to realize the high-dimensional quantum computation, which can advance the trend of exploring multi-DoF quantum resources of the atomic array. In order to consistently accommodate the two DoFs in a single setup, we come up with a ladder-shaped tweezer array (LTA) configuration, in which each rung of the ladder contains two tweezers and forms a cell of the setup. Loading one atom to each cell, the occupation of the atom in the two tweezers contributes to the SO DoF, and within each tweezer, the atom can occupy different Mo states, which is manifested as the Mo DoF. Both the SO and Mo DoF are applied to encode qubits, which enables each atom to carry two qubits. We further design the single-qubit rotational gates for the SO and Mo qubits, as well as the SO-SO, Mo-Mo, and SO-Mo CNOT gates for qubits belonging to the same and different DoFs, which transfers the LTA to a two-layer highly connected qubit architecture. We also assembled quantum circuits to generate the hyper- and hybrid-entanglements between the SO and Mo DoFs, which can be further applied to high-dimensional universal quantum computations.

This paper is organized as follows: Sect. 2 introduces the LTA system under consideration; Sect. 3 presents the single- and two-atom operation elements to the quantum gates, and the assembling of these operation elements to quantum gates is given in Sect. 4; The application of the quantum gates to generate the hyper- and hybrid entanglements is given in Sect. 5; in Sect. 6 the discussion of the experimental feasibility of the proposal is supplied; and a brief summary is given in Sect. 7.

## 2 The ladder-shaped atomic tweezer array

The spatial configuration of the ladder-shaped tweezer array (LTA) is depicted in Fig. 1(a), in which the leg and rung of the LTA are along the x- and y-direction, respectively. Each rung is composed of two tweezers lying close to each other and is taken as a supercell of the array, of which the filling of a single atom in each supercell is considered. The LTA contributes to the storage tweezer for atoms, and we also introduce the shuttle tweezers, which are movable and can transport atoms. We further consider that the storage and the shuttle tweezers can only trap atoms of a

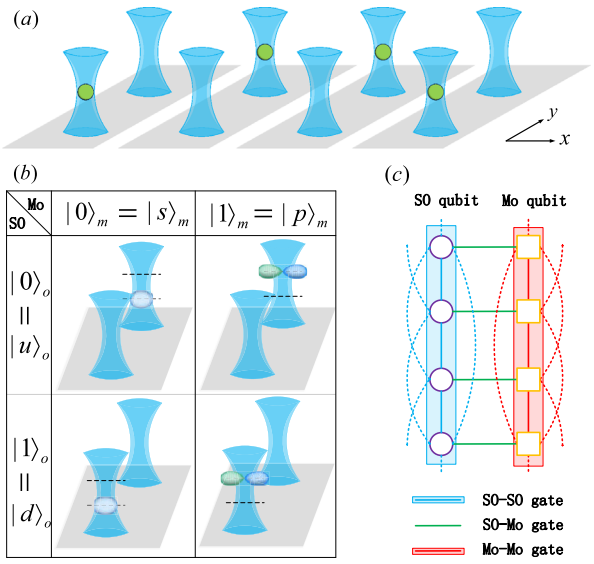


**Figure 1** The quantum computation platform of the ladder-shaped atomic array (LTA). (a) The sketch of the LTA setup with one atom trapped in each supercell. (b) The illustration of the qubits encoded in the SO and Mo DoF. (c) The two-layer highly-connected qubit architecture constructed from the LTA setup. The purple circles and yellow squares denote the SO and Mo qubits, respectively, and the blue, red, and green (dotted) lines connecting different qubits represent the two-qubit gates

particular spin state, i.e. the inner state of the atom, which can be realized by the state-dependent tweezers. The potential profile for both the storage and shuttle tweezers are given as:

$$V_{twz}[V_0, \vec{R}_0](\vec{r}) = V_0 e^{-2(x-x_0)^2/w_x^2 - 2(y-y_0)^2/w_y^2}, \tag{1}$$

where $V_0$ and $\vec{R}_0 = (x_0, y_0)$ denote the depth and the equilibrium position of the tweezer, respectively. $V_0$ can be dynamically controlled for both the storage and shuttle tweezers, while $\vec{R}_0$ is time-dependent for shuttle tweezers only, with $\vec{R}_0$ for the storage tweezer in the upper (lower) leg of the $j$-th cell fixed to position $\vec{R}_{j,u(d)} = (x_{j,u(d)}, y_{j,u(d)})$. The waists of all tweezers along the x- and y-direction are chosen unequal, i.e. $w_x \neq w_y$, to induce the anisotropy along the two directions. The state-dependent storage and shuttle tweezers are exerted on atoms in the spin states of $|\downarrow\rangle_s$ and $|\uparrow\rangle_s$, respectively.

Besides the spin states, atoms trapped in LTA also acquire various DoFs, such as the SO and Mo DoFs, providing rich resources for quantum computation. Given that each atom can only occupy the two tweezers in a particular supercell, the SO DoF of each is spanned by the occupation states of $\{|u\rangle_o, |d\rangle_o\}$, which specify the occupation of the atom in the up or down tweezer of the cell. Within a single tweezer, the atom can occupy different Mo states along

the x- and y-direction, and the anisotropy of the tweezers lifts the degeneracy and energetically decouples the Mo states in the two directions. In this work, we only consider the Mo states in the x-direction and fix the atom occupying the lowest Mo state in the y-direction. The two lowest Mo states in the x-direction in the tweezer are denoted as $|s\rangle_m$ and $|p\rangle_m$, which is referred to as the Mo DoF. In this way, each atom confined in a separate supercell resides in the single-particle Hilbert space of $\{|\vec{R}\rangle_o|\alpha\rangle_m|\sigma\rangle_s\}$, with $\vec{R} \in \{\vec{R}_{j,u}, \vec{R}_{j,d}\}$, $\alpha \in \{s,p\}$, and $\sigma \in \{\uparrow,\downarrow\}$, corresponding to the SO, Mo and spin DoF, respectively. In this work, we explore the Mo and SO DoF to encode the computational qubit, with the inner states working as ancillary DoF for the manipulation of the qubits. Each atom is then carrying two qubits, with the computational basis states $|0\rangle$ and $|1\rangle$ shown in Fig. 1(b).

Exploiting the SO and Mo DoF to encode qubits, the LTA is transferred to a two-layer qubit architecture, as shown in Fig. 1(c), in which the qubits in the first and second layers are the Mo (square nodes) and SO (circle nodes) qubits, respectively. In Fig. 1(c), the connection between SO and Mo qubits is realized by the intra-layer SO-SO (solid blue), the Mo-Mo (solid red) CNOT gates coupling atoms in neighbor supercells, as well as the inter-layer SO-Mo CNOT gates, which couple the two DoFs of the same atom. The dashed lines in Fig. 1(c) indicate that atoms can still directly couple to those not in the nearest neighbor supercells, by e.g. moving the corresponding two cells close by.

## 3 Operation elements for quantum gates

There have been various proposals to implement one- and two-qubit gates on qubits encoded in a single DoF of atoms, while these implementations cannot be directly applied in the presence of multiple DoFs, due to the crosstalk between different DoFs, which we term as the inter-DoF crosstalk in the following. The inter-DoF crosstalk is addressed in this work, and we propose the general strategy composed of the detuning engineering and the multi-chromatic Hamiltonian modulation to suppress the inter-DoF crosstalk. This strategy is explored for both the single- and two-qubit gates of the LTA setup, which can fulfill the need for universal high-dimensional quantum computation with the Mo and SO qubits. These gates are decomposed into a set of single- and two-atom operation elements. In this section, we introduce these operation elements, which can be assembled to realize the quantum gates for the universal high-dimensional quantum computation.

### 3.1 Single-atom elements

#### *3.1.1 Mo-maintained spin rotation*

The spin rotation operation takes place between the $|\downarrow\rangle_s$ and $|\uparrow\rangle_s$ states of a single atom, which is subject to a storage tweezer and a shuttle tweezer located at the same position. Since the storage and the shuttle tweezers can only trap the atom in the $|\downarrow\rangle_s$ and $|\uparrow\rangle_s$ states, respectively, the spin rotation also transfers the atom between the storage and the shuttle tweezers. The spin rotation is normally induced by the Rabi oscillation between the two spin states, e.g. through the two-photon Raman (TPR) transition. In the multi-DoF setup, the Rabi frequency of the spin rotation will become dependent on the Mo state, since atoms of different Mo states exhibit different spatial wavefunction, and consequently experience different interaction strengths with the Raman lasers. The Mo-dependent Rabi frequency is the major source for the inter-DoF crosstalk in the spin rotation operation. In order to circumvent this inter-DoF crosstalk, we firstly introduce the Mo-selective spin rotation, including the s-s, p-p, and s-p spin rotations. In the $\alpha-\alpha'$ spin rotation ($\alpha,\alpha' \in \{s,p\}$), the Rabi oscillation only takes place for the atom between $|\downarrow\rangle_s|\alpha\rangle_m$ and $|\uparrow\rangle_s|\alpha'\rangle_m$ states.

The Mo-selective spin rotation is composed of the detuning engineering of the states $|\sigma\rangle_s|\alpha\rangle_m$, where $\sigma \in \{\uparrow,\downarrow\}$ and $\alpha \in \{s,p\}$, and the monochromatic Hamiltonian modulation through e.g. the TPR process. The detuning engineering is introduced by assigning the shuttle and storage tweezers, with different depths of $V_{sh}$ and $V_{sg}$, respectively, with $V_{sh} \neq V_{sg}$. The unequal tweezer depth leads to the different energy detuning $\epsilon_{s,sh} - \epsilon_{s,sg} \neq \epsilon_{p,sh} - \epsilon_{p,sg}$, where $\epsilon_{\alpha,S}$ refers to the energy of the atom in the $\alpha \in \{s,p\}$ Mo state of the $S \in \{sh,sg\}$ tweezer. Consider the Rabi oscillation induced by the TPR process, which employs two lasers with frequency $\omega_1$ and $\omega_2$, respectively. Under the condition that $\hbar|\omega_1-\omega_2| = |\epsilon_{s,sh}-\epsilon_{s,sg}|$, the Raman lasers are only in resonance with the transition from $|\downarrow\rangle_s|s\rangle_m$ to $|\uparrow\rangle_s|s\rangle_m$, and will selectively induce the spin rotation for the atom in $|s\rangle_m$ Mo state, i.e. the s-s spin rotation. Similarly, applying the Raman lasers of $\hbar|\omega_1-\omega_2| = |\epsilon_{p,sh}-\epsilon_{p,sg}|$ will selectively induce the p-p spin rotation.

The $\alpha-\alpha$ spin rotation with $\alpha \in \{s,p\}$ can be described by the propagator as:

$$\hat{R}^{\alpha}_{spin}[\theta,\varphi] = |\alpha\rangle_m\langle\alpha| \otimes \left( [|\uparrow\rangle_s, |\downarrow\rangle_s] \overleftrightarrow{R}[\theta,\varphi] \begin{bmatrix} {}_s\langle\uparrow| \\ {}_s\langle\downarrow| \end{bmatrix} \right),$$
$$\overleftrightarrow{R}[\theta,\varphi] = \begin{bmatrix} \cos(\theta) & \sin(\theta)e^{-i\varphi} \\ \sin(\theta)e^{i\varphi} & -\cos(\theta) \end{bmatrix}, \tag{2}$$

where $\cos(\theta) = \frac{\delta_\alpha}{\sqrt{\delta_\alpha^2+\Omega_\alpha^2}}$, $\sin(\theta) = \frac{\Omega_\alpha}{\sqrt{\delta_\alpha^2+\Omega_\alpha^2}}$ and $\varphi = \varphi_\alpha$. In the above equations, $\delta_\alpha$ and $\Omega_\alpha$ denote the energy detuning from the intermediate state of the TPR process, and the Rabi frequency of the corresponding Raman laser, respectively, with $\varphi_\alpha$ the phase bias of the Raman lasers. $\delta_\alpha$ and $\Omega_\alpha$ can be controlled by the frequency and amplitude of the Raman lasers as in the normal two-photon Raman process. The operation time can be found as $T_\alpha = \frac{\pi}{\sqrt{\delta_\alpha^2+\Omega_\alpha^2}}$. The detailed derivation of $\hat{R}^{\alpha}_{spin}[\theta,\varphi]$ can be found in Appendix A.1. Figure 2 (a) and (b) illustrate the s-s and p-p

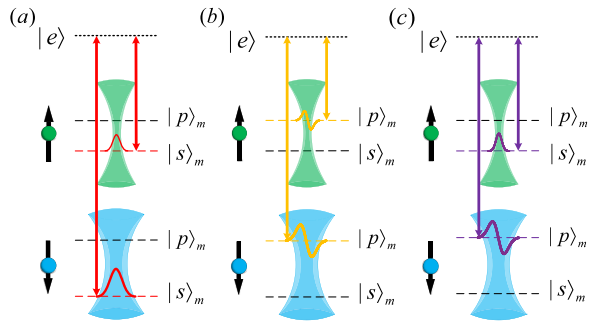


**Figure 2** Sketch of the Mo-maintained spin rotation for (a) s-s, (b) p-p and (c) s-p rotation channels. The atom of spin states $|\uparrow\rangle_s$ and $|\downarrow\rangle_s$ is trapped in the shuttle (upper row) and storage (bottom row) tweezers, respectively. The energy levels of the basis states under consideration are indicated by the dashed lines, with that of the intermediate states shown by dotted lines. Raman lasers are illustrated with vertical arrows

spin rotation through the two-photon Raman transition, respectively.

The s-p spin rotation can be realized by the two-photon Raman transition in which the laser frequency fulfills $\hbar|\omega_1 - \omega_2| = |\epsilon_{s,sh} - \epsilon_{p,sg}|$, and is of the similar mechanism as the Raman sideband cooling, which induces the state transfer between $|\uparrow\rangle_s|s\rangle_m$ and $|\downarrow\rangle_s|p\rangle_m$, as sketched in Fig. 2(c). The unitary propagator for the Raman sideband transition can be given as:

$$\begin{aligned}\hat{R}_{RSC}[\theta,\varphi] &= [|s\rangle_m|\uparrow\rangle_s, |p\rangle_m|\downarrow\rangle_s] \\ &\quad\times \overleftrightarrow{R}[\theta,\varphi]\begin{bmatrix} {}_m\langle s|_s\langle\uparrow| \\ {}_m\langle p|_s\langle\downarrow| \end{bmatrix} + \hat{P}_{RSC}, \\ \hat{X}_{RSC}(\vec{R}_1) &= \hat{R}_{RSC}[\frac{\pi}{2},0]\otimes|\vec{R}_1\rangle_o\langle\vec{R}_1| \\ &\quad + \hat{I}_m\otimes\hat{I}_{spin}\otimes(1-|\vec{R}_1\rangle_o\langle\vec{R}_1|),\end{aligned} \tag{3}$$

where $\hat{P}_{RSC} = [|s\rangle_m|\downarrow\rangle_s, |p\rangle_m|\uparrow\rangle_s]\times\begin{bmatrix} {}_m\langle s|_s\langle\downarrow| \\ {}_m\langle p|_s\langle\uparrow| \end{bmatrix}$.

The Mo-maintained spin rotation refers to the fact that the spin rotation is independent of the Mo state of the atom, and can be realized by the synchronized s-s and p-p spin rotation. The synchronization of the s-s and p-p spin rotations requires that the energy detuning from the intermediate state and the Rabi frequency of both rotations are the same, i.e. $\delta_s = \delta_p = \delta$ and $\Omega_s = \Omega_p = \Omega$. The synchronization condition can be achieved by two sets of the TPR processes, termed as the bi-TPR process, of which the first and second sets are composed of two Raman lasers of frequency $\{\omega_{s,1},\omega_{s,2}\}$ and $\{\omega_{p,1},\omega_{p,2}\}$, respectively. Under the condition that $\hbar|\omega_{s,1}-\omega_{s,2}| = |\epsilon_{s,sh}-\epsilon_{s,sg}|$ and $\hbar|\omega_{p,1}-\omega_{p,2}| = |\epsilon_{p,sh}-\epsilon_{p,sg}|$, the first and second set of Raman lasers will separately induce the s-s and p-p spin rotation, respectively, and the synchronization condition can be fulfilled by separately tuning the frequency and amplitude of the corresponding two lasers. The resultant propagator can be derived by the direct combination of $\hat{R}^s_{spin}[\theta,\varphi]$ and $\hat{R}^p_{spin}[\theta,\varphi]$, as:

$$\begin{aligned}\hat{R}_{spin}[\theta,\varphi] &= \hat{R}^s_{spin}[\theta,\varphi] + \hat{R}^p_{spin}[\theta,\varphi] \\ &= (|s\rangle_m\langle s| + |p\rangle_m\langle p|) \\ &\quad\otimes\left([|\uparrow\rangle_s,|\downarrow\rangle_s]\overleftrightarrow{R}[\theta,\varphi]\begin{bmatrix} {}_s\langle\uparrow| \\ {}_s\langle\downarrow| \end{bmatrix}\right) \\ &= \hat{I}_m\otimes[|\uparrow\rangle_s,|\downarrow\rangle_s]\overleftrightarrow{R}[\theta,\varphi]\begin{bmatrix} {}_s\langle\uparrow| \\ {}_s\langle\downarrow| \end{bmatrix},\end{aligned} \tag{4}$$

where $\hat{I}_m = |s\rangle_m\langle s| + |p\rangle_m\langle p|$.

Embedding the Mo-maintained Spin rotation in the complete LTA setup, this operation is applied to a particular atom trapped by a storage and a shuttle tweezer at the position of $\vec{R}_1$, is described by the corresponding propagator, as:

$$\begin{aligned}\hat{R}_{MmSF}[\theta,\varphi](\vec{R}_1) &= \hat{R}_{spin}[\theta,\varphi]\otimes|\vec{R}_1\rangle_o\langle\vec{R}_1| \\ &\quad + \hat{I}_m\otimes\hat{I}_{spin}\otimes(1-|\vec{R}_1\rangle_o\langle\vec{R}_1|),\end{aligned} \tag{5}$$

where $\hat{I}_{spin} = |\uparrow\rangle_s\langle\uparrow| + |\downarrow\rangle_s\langle\downarrow|$. We particularly introduce $\hat{X}_{MmSF}(\vec{R}_1) = \hat{R}_{MmSF}[\frac{\pi}{2},0](\vec{R}_1)$.

The Mo-maintained spin rotation transfers the atom from the storage to the shuttle tweezer and is accompanied by the spatial transport of the atom in the shuttle tweezer. The transport maintains the Mo state in the shuttle tweezer, and the propagator of the Mo-maintained transport is written as:

$$\hat{T}_{MmT}(\vec{R}_1\to\vec{R}_2;\sigma)|\alpha\rangle_m|\vec{R}_1\rangle_o|\sigma\rangle_s = |\alpha\rangle_m|\vec{R}_2\rangle_o|\sigma\rangle_s, \tag{6}$$

where $\alpha = s/p$ denotes Mo states and $\sigma = \downarrow / \uparrow$ denotes spin states. Given that the transport operation is only applied to the atom in the $|\uparrow\rangle_s$ state trapped in the shuttle tweezer, the propagator $\hat{T}_{MmT}(\vec{R}_1\to\vec{R}_2;\uparrow)$ can be simplified to $\hat{T}_{MmT}(\vec{R}_1\to\vec{R}_2)$, with the symbol for the spin state omitted. Combining the Mo-maintained (Mo-selective) spin-rotation and transport operations, we obtain the Mo-maintained (Mo-selective) shuttle operation, described by the unitary operators $\hat{X}_{MdS}(\vec{R}_1\to\vec{R}_2)$ ($\hat{X}_{MmS}(\vec{R}_1\to\vec{R}_2)$), which is defined as:

$$\begin{aligned}\hat{X}_{MdS}(\vec{R}_1\to\vec{R}_2) &= \hat{T}_{MmT}(\vec{R}_1\to\vec{R}_2)*\hat{X}_{RBC}(\vec{R}_1), \\ \hat{X}_{MmS}(\vec{R}_1\to\vec{R}_2) &= \hat{T}_{MmT}(\vec{R}_1\to\vec{R}_2)*\hat{X}_{MmSF}(\vec{R}_1).\end{aligned} \tag{7}$$

### *3.1.2 Mo-maintained SO rotation*

The SO rotation refers to the hopping of a single atom between the up and down tweezers in the same supercell. The inter-DoF crosstalk in the SO rotation arises from

the fact that the hopping atom can stay in different Mo states of the initial tweezer, and the temporal period for the hopping processes depends on the Mo state of the atom, which leads to the requirement of synchronizing the hopping processes for the atom in different Mo states.

To suppress this crosstalk, we adopt a similar strategy as that in the Mo-maintained spin rotation in the last section, and firstly introduce three types of Mo-selective SO rotations, including the s-s, p-p, and p-s hoppings. In the $\alpha_1 - \alpha_2$ hopping, with $\alpha_1, \alpha_2 \in \{s, p\}$, the hopping process can take place only between the $|\alpha_1\rangle_m$ state in the initial tweezer and the $|\alpha_2\rangle_m$ state in the target tweezer, with atoms in the other Mo state remaining in the initial tweezer. The atom hopping with the Mo state maintained, i.e., the Mo-maintained SO rotation, can be realized by the combination of the s-s and p-p hoppings, each of which transfers an atom in a single Mo state from the initial to the target tweezer.

The Mo-selective SO rotations can also be realized by the strategy of the detuning engineering accompanied by the monochromatic Hamiltonian modulation through the photon-assisted tunneling [28, 29], in which the periodic lattice shaking plays the role of an effective photon. The photon-assisted tunneling is capable of transferring an atom between two traps with the on-site energy detuning experienced by the hopping atom, which could be induced by the local interaction in one trap [28] and/or a lattice gradient [29]. In the Mo-selective SO rotations, the detuning engineering refers to setting the depths of the two tweezers differently, and consequently inducing the energy detuning between the Mo states in the two tweezers, i.e. $\epsilon_{\alpha_1,ini} \neq \epsilon_{\alpha_2,tar}$, where $\epsilon_{\alpha,ini(tar)}$ denotes the atom in $|\alpha\rangle_m$ state of the initial (target) tweezer of the hopping process, with $\alpha \in \{s, p\}$. More importantly, the potential depth difference induces the different energy detuning of $\Delta_{s-s} \neq \Delta_{p-p}$, with $\Delta_{s-s(p-p)} = \epsilon_{s(p),ini} - \epsilon_{s(p),tar}$. The photon-assisted tunneling through monochromatic shaking of the initial tweezer is then applied, and the exclusive hopping of the atom from the $|\alpha_1\rangle_m$ state in the initial tweezer to the $|\alpha_2\rangle_m$ state in the target tweezer can be induced by choosing the shaking frequency $\hbar\omega_{\alpha_1-\alpha_2} = \epsilon_{\alpha_1,ini} - \epsilon_{\alpha_2,tar}$, which is termed as the $\alpha_1 - \alpha_2$ hopping. Particularly, $(\alpha_1, \alpha_2) = (s, s)$, $(p, p)$ and $(p, s)$ refer to the s-s, p-p, and s-p hopping, as indicated by the red, orange, and purple arrows in Fig. 3(a), (b) and (c), respectively.

The energy detuning engineering with $\epsilon_{\alpha_1,ini} \neq \epsilon_{\alpha_2,tar}$ guarantees that the s-s, p-p and p-s hoppings fulfill different resonant shaking conditions, and cannot be activated under the same monochromatic shaking. The unitary propagator for the $\alpha_1 - \alpha_2$ hopping with evolution time $T_{\alpha_1-\alpha_2} = \frac{\pi}{\sqrt{\delta^2_{\alpha_1-\alpha_2} + \Omega^2_{\alpha_1-\alpha_2}}}$, where $\delta_{\alpha_1-\alpha_2}$ and $\Omega_{\alpha_1-\alpha_2}$ denote the energy detuning and Rabi frequency of the hopping, can be written as:

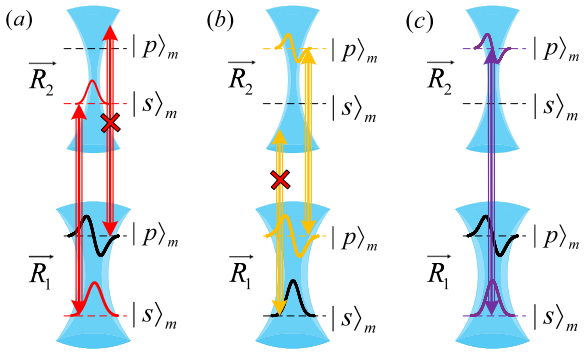


**Figure 3** Mo-dependent hopping with the (a) s-s, (b) p-p, and (c) s-p tunneling between the two tweezers located at $\vec{R}_1$ (bottom row) and $\vec{R}_2$ (upper row). The red, yellow, and purple arrows indicate the photo-assisted tunneling operation, through the lattice shaking of the tweezer at $\vec{R}_1$ with a particular frequency

$$\hat{R}_{SO}^{\alpha_1\to\alpha_2}[\theta,\varphi](\vec{R}_1 \to \vec{R}_2) = \Big(|\alpha_1\rangle_m|\vec{R}_1\rangle_o, |\alpha_2\rangle_m|\vec{R}_2\rangle_o] \overleftrightarrow{R}[\theta,\varphi]\begin{bmatrix} {}_m\langle\alpha_1|_o\langle\vec{R}_1| \\ {}_m\langle\alpha_2|_o\langle\vec{R}_2| \end{bmatrix} + (1-\hat{P}_{SO})\Big) \otimes \hat{I}_{spin}, \tag{8}$$

where $\hat{P}_{SO} = |\alpha_1\rangle_m\langle\alpha_1| \times |\vec{R}_1\rangle_o\langle\vec{R}_1| + |\alpha_2\rangle_m\langle\alpha_2| \times |\vec{R}_2\rangle_o\langle\vec{R}_2|$, $\cos(\theta) = \frac{\delta_{\alpha_1-\alpha_2}}{\sqrt{\delta^2_{\alpha_1-\alpha_2}+\Omega^2_{\alpha_1-\alpha_2}}}$, $\sin(\theta) = \frac{\Omega_{\alpha_1-\alpha_2}}{\sqrt{\delta^2_{\alpha_1-\alpha_2}+\Omega^2_{\alpha_1-\alpha_2}}}$, with $\varphi = \varphi_{\alpha_1-\alpha_2}$ determined by the bias phase of the tweezer shaking. The detailed derivation of $\hat{R}_{SO}^{\alpha\to\alpha'}[\theta,\varphi](\vec{R}_1 \to \vec{R}_2)$ can be found in Appendix A.2. By adjusting the depths and distances of the tweezers as well as the evolving time, one can induce the operations manifested as the Pauli-X gates, which are expressed as:

$$\hat{X}_{MdH}(\vec{R}_1,\alpha_1;\vec{R}_2,\alpha_2) = \hat{R}_{SO}^{\alpha_1\to\alpha_2}[\frac{\pi}{2},0](\vec{R}_1 \to \vec{R}_2), \tag{9}$$

where $\alpha_{1(2)}$ denotes the Mo states trapped in $\vec{R}_{1(2)}$.

The Mo-maintained SO rotation can be realized by simultaneously performing the s-s and p-p SO rotations in the synchronized manner, during which the atom can hop from the arbitrary superposition of Mo states in the initial tweezer to the same Mo superposition in the target tweezer, i.e., the Mo state is maintained during the hopping process. The synchronization of the s-s and p-p SO rotations can be realized by a multi-chromatic shaking of the form $A_1\cos(\omega_1 t + \varphi) + A_2\cos(\omega_2 t + \varphi)$. The two frequencies separately match the resonance conditions of the s-s and p-p hoppings, respectively, with $\hbar\omega_1 = \epsilon_{s,ini} - \epsilon_{s,tar}$ and $\hbar\omega_2 = \epsilon_{p,ini} - \epsilon_{p,tar}$. Meanwhile tuning the shaking amplitudes $A_1$ and $A_2$ can then selectively tune the Rabi frequencies of the s-s and p-p hoppings, respectively. The two hopping processes can then be synchronized, which gives

rise to the Mo-maintained SO rotation. The propagator of the Mo-maintained SO rotation can be expressed as:

$$\begin{aligned}&\hat{R}_{SO}[\theta,\varphi](\vec{R}_1;\vec{R}_2)\\&=\hat{R}_{SO}^{p\to p}[\theta,\varphi](\vec{R}_1\to\vec{R}_2)*\hat{R}_{SO}^{s\to s}[\theta,\varphi](\vec{R}_1\to\vec{R}_2)\\&=\hat{I}_m\otimes[|\vec{R}_1\rangle_o,|\vec{R}_2\rangle_o]\overleftrightarrow{R}[\theta,\varphi]\begin{bmatrix}{}_o\langle\vec{R}_1|\\{}_o\langle\vec{R}_2|\end{bmatrix}\otimes\hat{I}_{spin}.\end{aligned}\tag{10}$$

### *3.1.3 Mo rotation*

The rotation between different Mo states of one atom in a single tweezer can be realized by the periodic tweezer shaking, and is less affected by the inter-DoF crosstalk than the rotation of the spin and SO states, since the Mo-state rotation amplitude and temporal period are less dependent on the location and spin states of the atoms. Consider that the Mo rotation is applied to the atom trapped in a particular supercell of the LAT, shaking the two tweezers with the same amplitude, frequency, and biased phase can realize the SO-maintained Mo rotation, while the shaking of a single tweezer can directly be used as the inter-DoF CNOT gate, in which the control and target qubits are encoded in the SO and Mo DoF, respectively.

We take the single-tweezer shaking for instance, and consider a single atom confined in a storage tweezer, under the periodic modulation of the tweezer's equilibrium position, as

$$\begin{aligned}&\hat{V}_{Mo}=V_{twz}[V_{sg},(x_c(t),y_c)](\vec{r})\,|\downarrow\rangle_s\langle\downarrow|,\\&x_c(t)=x_c+\tilde{\Omega}_{Mo}\cos(\omega_{Mo}t+\varphi_{Mo}).\end{aligned}\tag{11}$$

In the above equation, $x_c$ ($y_c$) is the coordinate of the initial location of the tweezer along the x-coordinate (y-coordinate). The modulation frequency, amplitude, and the biased phase are given as $\omega_{Mo}$, $\tilde{\Omega}_{Mo}$ and $\varphi_{Mo}$, respectively. Under the resonant shaking condition where $\hbar\omega_{Mo}=\epsilon_{s,sg}-\epsilon_{p,sg}$, the atom in the storage tweezer is undergoing a Rabi-like oscillation between the $|s\rangle_m$ and $|p\rangle_m$ states, which is termed as the Mo rotation process. The propagator of the Mo rotation element is:

$$\hat{R}_{Mo}[\theta,\varphi]=[|s\rangle_m,|p\rangle_m]\overleftrightarrow{R}[\theta,\varphi]\begin{bmatrix}{}_m\langle s|\\{}_m\langle p|\end{bmatrix}\otimes\hat{I}_{spin},\tag{12}$$

where $\cos(\theta)=\frac{\delta_{Mo}}{\sqrt{\delta_{Mo}^2+\Omega_{Mo}^2}}$, $\sin(\theta)=\frac{\Omega_{Mo}}{\sqrt{\delta_{Mo}^2+\Omega_{Mo}^2}}$ and $\varphi=\varphi_{Mo}$, with the evolution time $T_{Mo}=\frac{\pi}{\sqrt{\delta_{Mo}^2+\Omega_{Mo}^2}}$. The detail definition of the detuning $\delta_{Mo}$, the Rabi frequency $\Omega_{Mo}$ and the biased phase $\varphi_{Mo}$ are given in Appendix A.3. Adjusting the modulation frequency, biased phase, and amplitude, different kinds of Mo rotation operations exerted on the position $\vec{R}_1$ can be realized, such as the Pauli-X element, which has:

$$\begin{aligned}\hat{R}_{Mo}[\theta,\varphi](\vec{R}_1)&=\hat{R}_{Mo}[\theta,\varphi]\otimes|\vec{R}_1\rangle_o\langle\vec{R}_1|\\&\quad+\hat{I}_m\otimes\hat{I}_{spin}\otimes(1-|\vec{R}_1\rangle_o\langle\vec{R}_1|),\\\hat{X}_{Mo}(\vec{R}_1)&=\hat{R}_{Mo}[\frac{\pi}{2},0](\vec{R}_1).\end{aligned}\tag{13}$$

## 3.2 Two-atom operation elements

Besides the single-qubit gates, universal quantum computation also requires entanglement generation gates between two qubits, e.g. the CNOT gate. In the multi-DoF LTA setup, the CNOT gates can be further specified as the intra-DoF CNOT gates with both the control and target qubits being the same DoF, denoted as the Mo-Mo and SO-SO CNOT gates, as well as the inter-DoF SO-Mo CNOT gate, with the control and target qubits being the SO and Mo qubits of the same atom. The intra-DoF SO-Mo CNOT gate has been introduced in Sect. 3.1.3, and the implementation of SO-SO and Mo-Mo CNOT gates also follows the strategy of the combination of the detuning engineering and the synchronization scheme through multi-chromatic Hamiltonian modulation. The energy detuning in both gates is engineered by the interaction between the control and target atoms, and the multi-chromatic Hamiltonian modulation is realized by the corresponding operation elements of the SO and Mo rotations.

### *3.2.1 Controlled Mo-maintained spin rotation*

The controlled Mo-maintained spin rotation is applied to a target atom. The tweezers trapping the target atom are composed of a storage and a shuttle tweezer located at the same position, from which a control tweezer is lying nearby. The controlled Mo-maintained spin rotation realizes the function that the spin rotation of the target atom can only take place when the control tweezer is not occupied by an atom. The controlled Mo-maintained spin rotation can then be demonstrated in the three-tweezer setup, which is composed of a storage and a shuttle tweezer for the target atom in different spin states, and a control tweezer, as illustrated in Fig. 4. The potential of the three-tweezer setup is given as:

$$\begin{aligned}\hat{V}_{CSF}&=V_{twz}[V_{sg},\vec{R}_1]\,|\downarrow\rangle_s\langle\downarrow|\\&\quad+V_{twz}[V_{sh},\vec{R}_1]\,|\uparrow\rangle_s\langle\uparrow|\\&\quad+V_{twz}[V_c,\vec{R}_2]\,|\uparrow\rangle_s\langle\uparrow|,\end{aligned}\tag{14}$$

in which the first and the second terms denote the storage and shuttle tweezer, respectively, located at $\vec{R}_1$, and the last term is the control tweezer located at $\vec{R}_2$. we assume that the control tweezer lies close to the storage and shuttle tweezer.

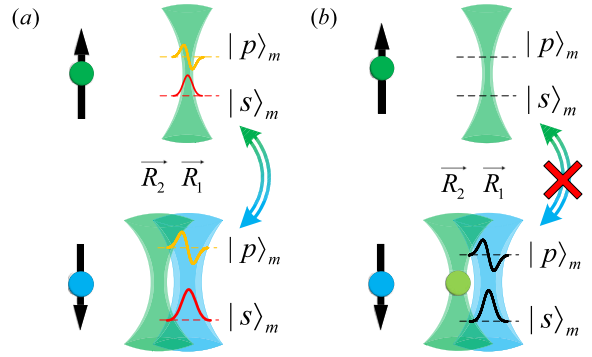


**Figure 4** The controlled Mo-maintained spin-rotation operation, with the storage (lower row) and shuttle tweezer (upper row) of the target atom located at $\vec{R}_1$ and the control tweezer located at $\vec{R}_2$. (a) Under the condition that the control tweezer is not loaded with an atom, the target atom in the storage tweezer can perform the Mo-maintained spin rotation, which is accompanied with the transfer of the target atom from the storage to the shuttle tweezer. (b) Under the condition that the control tweezer is loaded with an atom, the Mo-maintained SO rotation of the target atom is prevented by the atom-atom interaction

In the controlled Mo-maintained spin rotation, the detuning engineering is introduced by the interaction between the target atom and the atom in the control tweezer, denoted as $U^{\vec{R}_1,\vec{R}_2}_{\sigma,\sigma'}$, where $\sigma$ and $\sigma'$ refers to the spin state of the atom in the storage and control tweezer, respectively. The contact interaction is assumed to be spin-dependent, as $U^{\vec{R}_1,\vec{R}_2}_{\downarrow,\uparrow} \neq U^{\vec{R}_1,\vec{R}_2}_{\uparrow,\uparrow}$. The energy difference between the $|s\rangle_m$ ($|p\rangle_m$) in the storage and shuttle tweezers with the absence of an atom in the control tweezer is given as $\Delta_{s,0} = \epsilon_{s,sh} - \epsilon_{s,sg}$ ($\Delta_{p,0} = \epsilon_{p,sh} - \epsilon_{p,sg}$), and the corresponding energy difference between the $|s\rangle_m$ ($|p\rangle_m$) in the two tweezers with the control tweezer loaded with an atom is then given as $\Delta_{s,1} = \Delta_{s,0} + U^{\vec{R}_1,\vec{R}_2}_{\uparrow,\uparrow} - U^{\vec{R}_1,\vec{R}_2}_{\downarrow,\uparrow}$ ($\Delta_{p,1} = \Delta_{p,0} + U^{\vec{R}_1,\vec{R}_2}_{\uparrow,\uparrow} - U^{\vec{R}_1,\vec{R}_2}_{\downarrow,\uparrow}$).

Provided the detuning engineering by the interaction between the two atoms, the Mo-maintained spin rotation can be directly realized by the synchronized s-s and p-p spin rotation by the bi-TPR process as introduced in 3.1.1. The two TPR-laser sets are separately in resonance with $\Delta_{s,0}$ and $\Delta_{p,0}$, respectively, which can induce synchronized s-s and p-p spin rotation under the condition that the control tweezer is not loaded with an atom. The presence of an atom in the control tweezer, however, will change the energy detuning to $\Delta_{s(p),1}$, which is off-resonant with the TPR lasers and prevents the s-s and p-p spin rotations. The cooperation of the detuning engineering through the atom-atom interaction and the synchronized bi-TPR process gives rise to the controlled Mo-maintained spin rotation.

The controlled Mo-maintained spin rotation is then illustrated in Fig. 4, which shows that the Mo-maintained spin rotation of the target atom is permitted (Fig. 4 (a)) or suppressed (Fig. 4 (b)) with the control atom loaded or not in the control tweezer. The resultant propagator of the controlled Mo-maintained shuttling is given as

$$\hat{U}^C_{MmSF}(\vec{R}_1) = (1-\hat{n}_C)\otimes\hat{X}_{MmSF}(\vec{R}_1) + \hat{n}_C\otimes\hat{I}_{\vec{R}_1}, \tag{15}$$

where $\hat{n}_C$ denotes atom population number in the control shuttle tweezer in the $\vec{R}_2$ and is 1 or 0 depends the control tweezer contains atom or not, $\hat{I}_{\vec{R}_1}$ denotes unit operator to the states in the storage tweezer in $\vec{R}_1$. The potential depths of the control tweezer and the shuttle tweezer, $V_C$ and $V_{sh}$, are adjusted mismatch to stop tunneling between these two tweezers, as shown in Fig. 4.

### 3.2.2 *Controlled Mo-maintained SO rotation*

The controlled Mo-maintained SO rotation also involves a three-tweezer setup, of which two storage tweezers hold a target atom and a shuttle tweezer plays the role of the control tweezer. The SO rotation refers to the hopping of the target atom between the two storage tweezers, and the process is determined by whether an atom is present in the control tweezer or not. The absence (presence) of the atom in the control tweezer will permit (prevent) the Mo-maintained hopping of the target atom. In order to realize the controlled Mo-maintained SO rotation, we engineer the energy detuning by both the depth difference between the two storage tweezers and the interaction between the target atom and the atom in the control tweezer. The synchronized hopping of the target atom is realized through the multi-chromatic photon-assisted tunneling as introduced in 3.1.2. in the control tweezer is $\Delta_{\alpha-\alpha}$ ($\Delta_{\alpha-\alpha,1} = \Delta_{\alpha-\alpha} + U_\alpha$) defined in 3.1.2, where $U_\alpha$ is the interaction strength with the target atom in the $|\alpha\rangle_m$ state. The photon-assisted tunneling is then done with the shaking of the storage tweezer where the target atom is initially located, with the function of $A_1 cos(\omega_1 t + \varphi) + A_2 cos(\omega_2 t + \varphi)$, of which the shaking frequency $\omega_{1(2)} = \Delta_{s-s(p-p)}/\hbar$ to ensure that only the absence of an atom in the control tweezer can permit the Mo-maintained hopping, with the value of $A_{1(2)}$ realizing the synchronization condition. The controlled Mo-maintained SO rotation refers to that the s-s hopping between the target and goal tweezers can (cannot) take place in the absence (presence) of one atom in the control tweezer, as sketched in Fig. 5(a) (Fig. 5(b)). This operation also resembles the interaction controlled Josephson junction [30], in which the tunneling of the atom in a double well is determined by whether an ion is lying in between the two wells. Consider the case of a single control tweezer, the corresponding propagator reads:

$$\begin{aligned}\hat{U}^C_{MdH}(\vec{R}_1,\alpha_1;\vec{R}_2,\alpha_2) &\\ = (1-\hat{n}_C)\otimes\hat{X}_{MdH}(\vec{R}_1,\alpha_1;\vec{R}_2,\alpha_2) &\\ + \hat{n}_C\otimes\hat{I}_{\vec{R}_1;\vec{R}_2}, &\end{aligned} \tag{16}$$

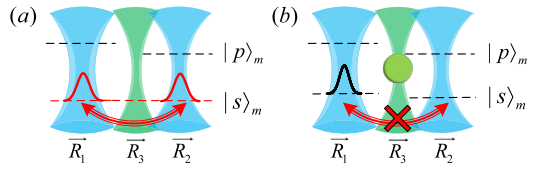


**Figure 5** The Controlled Mo-dependent hopping, with the control tweezer lying in between the target and the goal tweezers. (a) Under the condition that the control tweezer is not loaded with an atom, then s-s hopping takes place between the target and the goal tweezers. (b) The presence of an atom in the control tweezer prevents the s-s hopping between the target and the goal tweezers

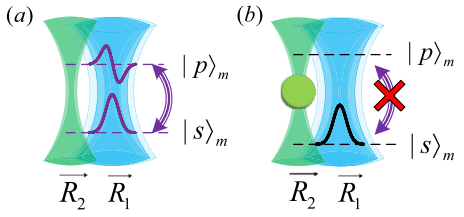


**Figure 6** Controlled Mo rotation operation with the target and control tweezers located at $\vec{R}_1$ and $\vec{R}_2$, respectively. (a) In the absence of an atom in the control tweezer, the atom in the target tweezer can perform the Mo rotation, driven by the periodic modulation of the target tweezer. (b) In the presence of an atom in the control tweezer, the Mo rotation in the target tweezer is prevented by atom-atom interaction between the two tweezers

in which $\vec{R}_1$, $\vec{R}_2$ and $\vec{R}_3$ are the locations of the initial, the target, and the control tweezer, respectively. $\hat{I}_{\vec{R}_1;\vec{R}_2}$ denotes the unit operator for the states in the two target tweezers. The controlled Mo-maintained SO rotation can be generalized to a setup with two control tweezers located at $\vec{R}_3$ and $\vec{R}_4$, in which one atom presenting in either of the two control tweezers will prevent the Mo-maintained SO rotation of the target atom.

### 3.2.3 *Controlled Mo rotation*

The Mo rotation refers to switching the Mo states of the target atom confined in the storage tweezer controlled by the presence and/or absence of an atom in the control tweezer lying nearby. The potential for the coexistence of the control and target tweezers is given as:

$$\begin{aligned}\hat{V}_{CMF} = {} & V_{twz}[V_{sg}, \vec{R}_1](\vec{r})\,|{\downarrow}\rangle_s\,\langle{\downarrow}| \\ & + V_{twz}[V_C, \vec{R}_2](\vec{r})\,|{\uparrow}\rangle_s\,\langle{\uparrow}|\,,\end{aligned} \tag{17}$$

in which the storage and control tweezer are lying at $\vec{R}_1$ and $\vec{R}_2$, respectively, with the control tweezer exerted to the atom in $|{\downarrow}\rangle_s$ state. Similar to the controlled Mo-maintained shuttling, the atom in the storage tweezer can undergo the Mo rotation through the resonant tweezer shaking, as sketched in Fig. 6(a), with no atom loaded in the control tweezer. The presence of one atom in the control tweezer, however, will induce a Mo-dependent interaction energy to the atom in the storage tweezer, and the energy difference between the Mo states will be off-resonant with the tweezer shaking frequency, which will suppress the flipping of the Mo states, as sketched in Fig. 6(b). The corresponding propagator of the controlled Mo rotation then reads:

$$\hat{U}^{C}_{MF}(\vec{R}_1) = (1-\hat{n}_C)\otimes\hat{X}_{Mo}(\vec{R}_1) + \hat{n}_C\otimes\hat{I}_{\vec{R}_1} \tag{18}$$

where $\hat{n}_{\vec{C}}$ denotes the atom population number in the control tweezer in $\vec{R}_2$, $\hat{I}_{\vec{R}_1}$ denotes unit operator of the target tweezer in $\vec{R}_1$. Alternatively, tuning the shaking frequency in resonance with the energy difference between the initial and final states of the target atom, which is subjected to the interaction from one atom in the control tweezer, one can realize the control scheme that the Mo rotation of the target atom can only take place in the presence of one atom in the control tweezer, as described by:

$$\hat{U}^{\overline{C}}_{MF}(\vec{R}_1) = \hat{n}_C\otimes\hat{X}_{Mo}(\vec{R}_1) + (1-\hat{n}_C)\otimes\hat{I}_{\vec{R}_1}\,. \tag{19}$$

The controlled Mo rotation can also be generalized to the situation with two control tweezers, specified with their location of $\vec{R}_2$ and $\vec{R}_3$, which are both close to the storage tweezer at $\vec{R}_1$. Under the condition that at most one atom will occupy the two control tweezers, with $n_C = n_{\vec{R}_2} + n_{\vec{R}_3} \in \{0,1\}$, ($n_{\vec{R}_{2(3)}}$ denotes the atom occupation in the control tweezer located at $\vec{R}_{2(3)}$).

## 3.3 Numerical verifications

In the above two sections, we have introduced the single- and two-atom operation elements to design the quantum gates required by the high-dimensional universal quantum computation. These elements, for one thing, generalize the standard operations, such as the two-photon Raman process and the photon-assisted tunneling from standard monochromatic to the multi-chromatic synchronized scheme, and for another, adapts the tweezer transport of atoms in the $|p\rangle_m$ Mo state. It is then necessary to numerically verify the feasibility of the multi-chromatic synchronization scheme, and the stability of the $|p\rangle_m$ Mo state during the transport by moving the tweezer. In this section, we take the Mo-maintained spin rotation for example to numerically verify the synchronization scheme, and also numerically demonstrate the stability of the $p$ Mo state during the tweezer transport. The numerical simulations are done with the ab initio method multi-layer multi-configuration time-dependent Hartree method for arbitrary species (ML-MCTDHX) [31–33], and the first-principle simulation with the method can well resolve the Mo states and their response to temporal modulation to

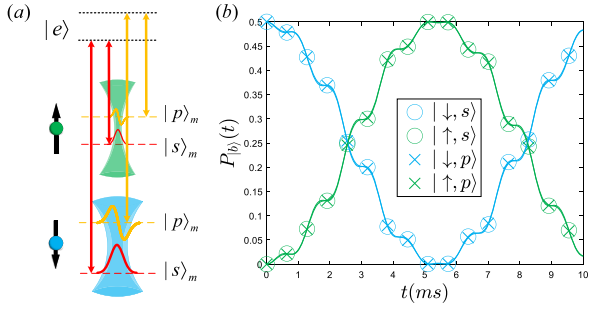


**Figure 7** Numerical verification of the synchronization scheme of the Mo-maintained spin rotation. (a) Sketch of the Mo-maintained spin rotation scheme through two sets of Raman lasers, denoted by the red and yellow arrows, respectively. (b) The temporal evolution of the basis-state Probability $P_{|b\rangle}(t)$ with $|b\rangle = |\downarrow\rangle_s |s\rangle_m$ (blue circle), $|b\rangle = |\uparrow\rangle_s |s\rangle_m$ (green circle), $|b\rangle = |\downarrow\rangle_s |p\rangle_m$ (blue cross), and $|b\rangle = |\uparrow\rangle_s |p\rangle_m$ (green cross). The blue and green lines are a guide to the eye

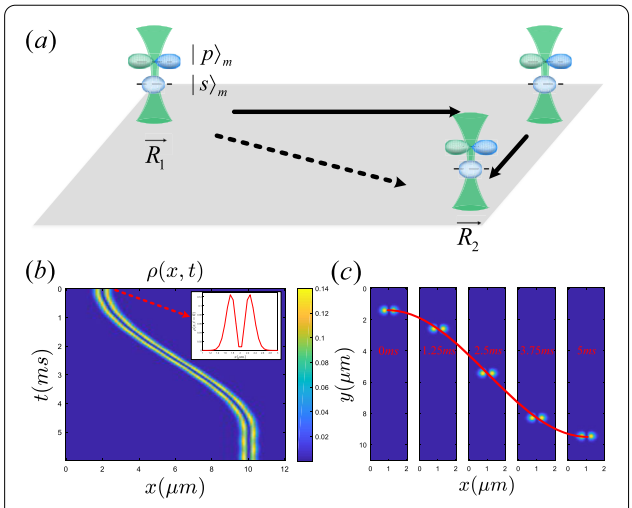


**Figure 8** Numerical verification of the stability of the atom in the $|p\rangle_m$ state during the transport process. (a) The sketch of the two-piece trajectory from the initial position $\vec{R}_1$ to the target position $\vec{R}_2$, which is illustrated with the solid arrows. (b) and (c) shows the one-body density of the atom under the transport along the x direction and y direction, respectively, which is initially prepared in the $|p\rangle_m$ state. The inset of (b) shows the one-body density of the initial state of the atom under transport. In (c), each panel plots the one-body density at a particular time, which is given in the inset of each panel, and the red line crossing different panels illustrates the trajectory $\vec{R}_c(t)$

the tweezers. In particular, the leakage of the Mo states out of the computational basis $\{|s\rangle_m, |p\rangle_m\}$ can be captured by the temporal modification of the spatial wavefunction of the atom by the method. A brief introduction to the method and the numerical setup is given in the Appendix C.

Figure 7 presents the Mo-maintained spin rotation through four Raman lasers. The coupling between different basis states by the four Raman lasers is sketched in Fig. 7(a), in which the coupling channels for the s-s and p-p spin rotations are illustrated with the red and yellow vertical arrows, respectively. The temporal evolution of the probability $P_{|b\rangle}(t)$ for the basis states $|b\rangle \in \{|\downarrow\rangle_s |s\rangle_m, |\uparrow\rangle_s |s\rangle_m, |\downarrow\rangle_s |p\rangle_m, |\uparrow\rangle_s |p\rangle_m\}$, are shown in Fig. 7(b). In the figure we can find that probability evolution of $|\downarrow\rangle_s |s\rangle_m$ ($|\uparrow\rangle_s |s\rangle_m$) coincides with that of $|\downarrow\rangle_s |p\rangle_m$ ($|\uparrow\rangle_s |p\rangle_m$), which directly verifies the validity of the synchronization scheme. Quantitatively speaking, the numerical simulation indicates that the Mo-maintained spin rotation can achieve a fidelity > 99% under an operation time around $5ms$ (the parameters are given in detail in Appendix C). The residual infidelity of the numerical simulation is attributed to the leakage to the higher excited Mo states out of the computational basis spanned by $\{|s\rangle_m, |p\rangle_m\}$, which can be faithfully captured by the temporal updating of the spatial wavefunction of the tweezer atoms implemented in ML-MCTDHX. The performance can be further improved by the optimal control scheme [17], of which system parameters, e.g. the amplitude and the biased phase of the Raman lasers are temporally optimized to reduce the operation time while maintaining the high fidelity.

The stability of the $|p\rangle_m$ Mo state during the atom transport by moving the tweezer is numerically verified, and the results are shown in Fig. 8. As depicted in Fig. 8(a), any transport from initial location $\vec{R}_1$ to the goal location of $\vec{R}_2$ can be realized by the two-piece trajectory, with the first and second piece of the trajectory along the x- and y-direction, respectively. Figures 8(b) and (c) show the one-body density of the atom at different times during the transport along the x- and y-direction, respectively, and particularly, the trajectories along both directions follow the sinusoidal function as $\vec{R}_c(t) = \vec{R}_{ini} + \left(\vec{R}_{fin} - \vec{R}_{ini}\right)[sin(\pi t/T - \pi/2) + 1]/2$, where $\vec{R}_{ini}$ ($\vec{R}_{fin}$) denotes the initial (final) location of the trajectory. It can be found that the Mo state of $|p\rangle_m$ remains stable during the transport along both directions, which guarantees that the transport of the atom between any two locations can maintain the Mo state by the two-piece trajectory. Quantitatively, the numerical simulation indicates that the fidelity of the atom remaining in the $|p\rangle_m$ state can reach > 99% during a transport time around $T = 5ms$ over a distance of $8\mu m$. The sinusoidal trajectory presents a more stable transport of the tweezer atom in the $|p\rangle_m$ state than the linear one, as compared in Appendix C, and it also suggests that the optimization of the trajectory can further improve the efficiency and the stability of the Mo-maintained shuttling [34].

**Table 1** Quantum gates' operations

| Quantum gate | | Operation |
|---|---|---|
| Single-qubit rotation gate | SO | $\hat{R}_{MmSF}[\theta,\varphi](\vec{R}) + \hat{X}_{MmS}(\vec{R}_2 \to \vec{R}_1)$ |
| | | $\hat{R}_{SO}[\theta,\varphi](\vec{R}_1;\vec{R}_2)$ |
| | Mo | $\hat{R}_{Mo}[\theta,\varphi](\vec{R})$ |
| Two-qubit CNOT gate | SO-Mo | $\hat{X}_{Mo}(\vec{R})$ |
| | SO-SO | $\hat{U}^C_{MmSF}(\vec{R}) + \hat{X}_{MmS}(\vec{R}_2 \to \vec{R}_1)$ |
| | | $\hat{U}^C_{MdH}(\vec{R}_1,\alpha;\vec{R}_2,\alpha) + \hat{X}_{MmS}(\vec{R}_2 \to \vec{R}_1)$ |
| | Mo-Mo | $\hat{U}^C_{MF}(\vec{R}) + \hat{X}_{MdS}(\vec{R}_2 \to \vec{R}_1) + \hat{T}_{MmT}(\vec{R}_2 \to \vec{R}_1)$ |

## 4 Quantum gates

In this section, we introduce the necessary single- and two-qubit gates for the high-dimensional universal quantum computation with the integration of the Mo and SO DoF. The single-qubit gates include the arbitrary rotation gates for the Mo and SO qubits. The two-qubit gates are chosen as the SO-Mo, SO-SO, and Mo-Mo CNOT gates, among which the SO-Mo CNOT gate is applied to the Mo and SO states of the same atom, and the SO-SO (Mo-Mo) CNOT gates are applied to the SO (Mo) qubits of two atoms. The single- and two-qubit gates can be assembled by the operation elements introduced in the previous section, and in the following, we will demonstrate the fabrication of the quantum gates through the related operation elements. The correspondence between the quantum gates and the operation elements is illustrated in Table 1.

*SO rotation gates*, such as the Pauli and Hadamard gates, can be realized by the Mo-maintained shuttling elements. The Pauli and Hadamard gates on the SO DoF of the $j$-th cell can be simultaneously realized by the rotation operation $\hat{\mathcal{U}}^j_{SO}[\theta,\varphi]$, as:

$$\begin{aligned}\hat{\mathcal{X}}^j_{SO} &= \hat{\mathcal{U}}^j_{SO}[\frac{\pi}{2},0],\\ \hat{\mathcal{H}}^j_{SO} &= \hat{\mathcal{U}}^j_{SO}[\frac{\pi}{4},0],\end{aligned} \tag{20}$$

where $\hat{\mathcal{X}}$ and $\hat{\mathcal{H}}$ separately denote Pauli-X gate and Hadamard gate.

The rotation operation $\hat{\mathcal{U}}^j_{SO}[\theta,\varphi]$ can be realized by the Mo-maintained shuttling operation, and assembled by the operation elements of

$$\begin{aligned}\hat{\mathcal{U}}^j_{SO}[\theta,\varphi] = \hat{X}_{MmS}(\vec{R}_{j,u} \to \vec{R}_{j,d})^{-1} * \hat{R}_{MmSF}[\theta,\varphi](\vec{R}_{j,d})\\ * \hat{X}_{MmS}(\vec{R}_{j,u} \to \vec{R}_{j,d}),\end{aligned} \tag{20}$$

where $\vec{R}_{j,u(d)}$ denotes the locations of the $y = u(d)$ tweezer in the $j$-th cell, and $\hat{X}_{MmS}(\vec{R}_{j,u} \to \vec{R}_{j,d})^{-1}$ is the inverse operation of $\hat{X}_{MmS}(\vec{R}_{j,u} \to \vec{R}_{j,d})$.

Another rotation operation $\hat{\mathcal{U}}^j_{SO}[\theta,\varphi]$ can be realized by the Mo-maintained SO rotation operation, which has:

$$\hat{\mathcal{U}}^j_{SO}[\theta,\varphi] = \hat{R}_{SO}[\theta,\varphi](\vec{R}_{j,u};\vec{R}_{j,d}), \tag{21}$$

where $\vec{R}_{j,u(d)}$ denotes the locations of the $y = u(d)$ tweezer in the $j$-th cell.

*Mo rotation gates* and the *SO-Mo CNOT gate* can be fabricated by the Mo rotation element and the periodic shaking applied simultaneously and identically to the two tweezers in the same cell realizes the single-qubit rotation gates on the Mo DoF. The Rotation operation on the Mo DoF of the atom in the $j$-th cell can then be assembled as

$$\hat{\mathcal{U}}^j_{Mo}[\theta,\varphi] = \hat{R}_{Mo}[\theta,\varphi](\vec{R}_{j,d}) * \hat{R}_{Mo}[\theta,\varphi](\vec{R}_{j,u}). \tag{22}$$

Choosing different parameters of $\theta$ and $\varphi$, one can realize the Pauli and Hadamard gates for the Mo DoF, as:

$$\begin{aligned}\hat{\mathcal{X}}^j_{Mo} &= \hat{\mathcal{U}}^j_{Mo}[\frac{\pi}{2},0],\\ \hat{\mathcal{H}}^j_{Mo} &= \hat{\mathcal{U}}^j_{Mo}[\frac{\pi}{4},0].\end{aligned} \tag{23}$$

SO-Mo CNOT gate applied to the two DoFs of a single atom can be realized by the X-type Mo rotation element on a single tweezer, which induces the SO-control Mo-NOT gate, as:

$$\hat{\mathcal{C}}^{j,y}_{SO-Mo} = \hat{X}_{Mo}(\vec{R}_{j,y}), \tag{24}$$

where $y = u/d$ denotes in which tweezer the atom will experience the Mo rotation.

*SO-SO CNOT gate* is applied to two atoms in different cells, and realizes the function that the SO state flipping of the target atom is determined by the SO state of the control atom. The SO-SO CNOT gate is then realized through the combination of the Mo-maintained shuttling of the control atom to the nearby of the target atom, and the controlled Mo-maintained hopping of the target atom, with the corresponding unitary operator is given as:

$$\begin{aligned}\hat{\mathcal{C}}^{j_1,j_2}_{SO-SO} &= \hat{X}^{j_1,j_2}_{dMmS}{}^{-1} * \hat{U}^C_{MmSF}(\vec{R}_{j_1,d};\vec{R}_{j_1,\tilde{d}}) * \hat{X}^{j_1,j_2}_{dMmS},\\ \hat{X}^{j_1,j_2}_{dMmS} &= \hat{X}_{MmS}(\vec{R}_{j_2,u} \to \vec{R}_{j_1,\tilde{d}}) * \hat{X}_{MmS}(\vec{R}_{j_1,u} \to \vec{R}_{j_1,d}),\end{aligned} \tag{25}$$

where $j_1$ and $j_2$ separately denote the target and control cells exerted two-qubit gate operations, $\vec{R}_{j_1,\tilde{d}}$ denotes the position close to $\vec{R}_{j_1,d}$ to induce interaction-control spin-flipping. The operator $\hat{U}^{j_1,j_2}_{dMmS}$ is double Mo-maintained shuttling acting on two tweezers, which are separately from the $j_1$ and $j_2$ cells. Alternatively, the SO-SO CNOT

gate can utilize the controlled Mo-dependent hopping elements, as:

$$\begin{aligned}\hat{\mathcal{C}}^{j_1,j_2}_{SO-SO} &= \hat{X}_{MmS}(\vec{R}_{j_2,u} \to \vec{R}_{j_1,\tilde{y}_c})^{-1} \\ &\quad * \hat{U}^{C;j_1,j_2}_{dMdH} * \hat{X}_{MmS}(\vec{R}_{j_2,u} \to \vec{R}_{j_1,\tilde{y}_c}), \\ \hat{U}^{C;j_1,j_2}_{dMdH} &= \hat{U}^{C}_{MdH}(\vec{R}_{j_1,d}, s; \vec{R}_{j_1,u}, s) * \hat{U}^{C}_{MdH}(\vec{R}_{j_1,d}, p; \vec{R}_{j_1,u}, p),\end{aligned} \tag{26}$$

where $\vec{R}_{j_1,\tilde{y}_c}$ denotes the center position between $\vec{R}_{j_1,u}$ and $\vec{R}_{j_1,d}$, serving for controlled Mo-dependent hopping operations. The operator $\hat{U}^{C;j_1,j_2}_{dMdH}$ is used to independently tunnel s and p Mo states between two target tweezers if the control tweezer is empty. Otherwise, the tunneling between two target tweezers will be prevented. Then depending on the site-occupation in the $j_2$ cell, we can control SO-flipping in the $j_1$ cell.

*Mo-Mo CNOT gate* can be realized by the combination of the Mo-dependent transfer and controlled Mo rotation elements. Mo-dependent transfer elements are used to transfer p Mo states in the $j_2$ cell to control tweezers. Then two control tweezers of the up and down occupation for the R-cell are moved around up and down storage tweezers in the $j_1$ cell, respectively when controlled Mo rotation elements are acting on them. Thus only when the $j_2$ cell atom occupies the s Mo state, the $j_1$ cell atom's Mo state will be flipped. The unitary operator of the motional-motional two-qubit gate thus has:

$$\begin{aligned}\hat{\mathcal{C}}^{j_1,j_2}_{Mo-Mo} &= \hat{X}^{j_1,j_2;d}_{dMdS} * \hat{U}^{C;j_1,j_2}_{dMF} * \hat{X}^{j_1,j_2;u}_{dMdS}, \\ \hat{X}^{j_1,j_2;y}_{dMdS} &= \hat{X}_{MdS}(\vec{R}_{j_2,d} \to \vec{R}_{j_1,\tilde{y}_2}) * \hat{X}_{MdS}(\vec{R}_{j_2,u} \to \vec{R}_{j_1,\tilde{y}_1}), \\ \hat{U}^{C;j_1,j_2}_{dMF} &= \hat{U}^{\overline{C}}_{MF}(\vec{R}_{j_1,d}) * \hat{T}^{j_1}_{dMmT} * \hat{U}^{\overline{C}}_{MF}(\vec{R}_{j_1,u}), \\ \hat{T}^{j_1}_{dMmT} &= \hat{T}_{MmT}(\vec{R}_{j_1,\tilde{u}_2} \to \vec{R}_{j_1,\tilde{d}_2}) * \hat{T}_{MmT}(\vec{R}_{j_1,\tilde{u}_1} \to \vec{R}_{j_1,\tilde{d}_1}),\end{aligned} \tag{27}$$

where $\hat{X}^{j_1,j_2;y}_{dMdS}$ denotes the double Mo-dependent shuttling operations, which is used to transport p Mo states of the $j_2$ cell to shuttle tweezers and move to $\vec{R}_{j_1,\tilde{y}}$ which is around $\vec{R}_{j_1,y}$ as control cells. $\hat{U}^{C;j_1,j_2}_{dMF}$ is used to perform controlled Mo rotation separately for the up and down tweezers. $\hat{T}^{j_1}_{dMmT}$ is used to move two control tweezers into the position around the target tweezer for the controlled Mo rotation operation.

## 5 Quantum circuits

The ultra-cold atoms trapped in the optical tweezer system possess the capabilities of both efficient parallel operations and high-fidelity individual manipulations. Let us first focus on the basic quantum gates for quantum computing, which include all single qubit rotations(including Hadamard) and CNOT operations. For this ultra-cold atomic system, these qubits are encoded into SO and Mo DoF, which could be described as ladder-like connected devices due to unique connection patterns between these qubits. The two-qubit gates that link these qubits distributed in this ladder-like connected devices can be mainly divided into two categories: intra two-qubit gates and inter two-qubit gates, which are the intrinsic factors of hyper and hybrid nonlocality [35]. This system has excellent scalability, for $2n$ qubits encoded on $n$ atomic tweezers array, which could be seen as two independent linear nearest neighbor connected devices, and the topology of this ladder-like tweezer array and the number of qubits are illustrated in Fig. 9(a): one is constructed by SO-qubit-chain $q_0, q_2, \ldots, q_{2n-2}$, which are denoted by circles and the correlation with the adjacent qubit could be resulted by the SO-SO gate $\hat{\mathcal{C}}^{i,j}_{SO-SO}$, the other is constituted by Mo-qubit-chain $q_1, q_3, \ldots, q_{2n-1}$, which are denoted by squares and could be entangled with the nearest Mo-qubit through the Mo-Mo gate $\hat{\mathcal{C}}^{i,j}_{Mo-Mo}$. More importantly, the SO-Mo gate $\hat{\mathcal{C}}^{j,y}_{SO-Mo}$ creates a powerful hybrid correlation between these two different qubit-chains, which is the intrinsic motivation of this system's capability to perform multi-DoF quantum computation.

We could employ the set of multi-DoF gates to construct the quantum circuits required for quantum computing tasks, such as quantum Fourier transform [36, 37], Jordan–Wigner String [38, 39], Grover's diffusion operator [40, 41], quantum error correction codes [42–44], and so on. The ability to create multi-qubit entanglement serves as an important benchmark for quantum technologies, here we construct quantum circuits required for the preparation of multiple entangled states by simultaneously exploiting two different DoFs. Multi-DoF entanglement is divided into the following types [45]: hyper-entanglement, hybrid-entanglement, and hyper-hybrid entanglement. Among these multi-DoF entanglements, hyper-entanglement and hyper-hybrid entanglement possess higher entanglement degrees and better application scenarios and could be written as:

$$\begin{aligned}|\psi\rangle_{\text{hyper}} &= |GHZ\rangle_o \otimes |GHZ\rangle_m, \\ |GHZ\rangle_o &= \frac{1}{\sqrt{2}}(|0\rangle_o^{\otimes n} + |1\rangle_o^{\otimes n}), \\ |GHZ\rangle_m &= \frac{1}{\sqrt{2}}(|0\rangle_m^{\otimes n} + |1\rangle_m^{\otimes n});\end{aligned} \tag{28}$$

$$\begin{aligned}|\psi\rangle_{\text{hyper-hybrid}} &= \frac{1}{\sqrt{2}}(|0\rangle^{\otimes 2n} + |1\rangle^{\otimes 2n}), \\ |0\rangle^{\otimes 2n} &= |0\rangle_o^{\otimes n} \otimes |0\rangle_m^{\otimes n}, \\ |1\rangle^{\otimes 2n} &= |1\rangle_o^{\otimes n} \otimes |1\rangle_m^{\otimes n}.\end{aligned} \tag{29}$$

In Eq. (28), $|GHZ\rangle_o$ and $|GHZ\rangle_m$ represent maximally entangled GHZ states at SO and Mo DoF, respectively, and n

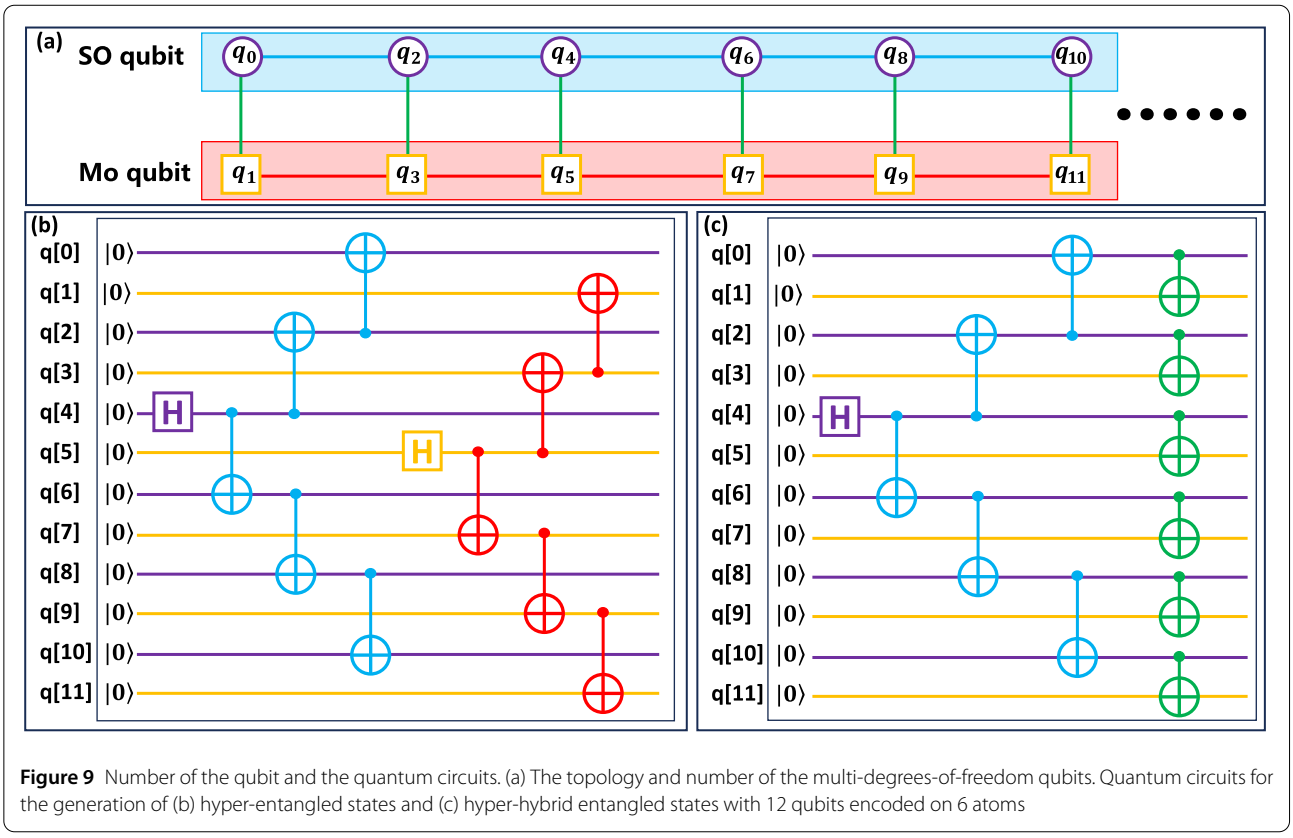


**Figure 9** Number of the qubit and the quantum circuits. (a) The topology and number of the multi-degrees-of-freedom qubits. Quantum circuits for the generation of (b) hyper-entangled states and (c) hyper-hybrid entangled states with 12 qubits encoded on 6 atoms

is the number of atoms. In Eq. (29), $|0\rangle^{\otimes 2n}$ as well as $|1\rangle^{\otimes 2n}$ represent $2n$ qubits global vector.

For both Eq. (28) and Eq. (29), starting with all atoms loaded in different cells are trapped in the same SO and Mo state,

$$|\psi\rangle_{ini} \equiv |0\rangle^{\otimes 2n} = |0\rangle_o^{\otimes n} \otimes |0\rangle_m^{\otimes n}, \tag{30}$$

and design a specific quantum circuit with $n = 6$, which are shown in Fig. 9(b) and 9(c), respectively. Both quantum circuits are optimal circuit depth for our system and could be decomposed into single qubit rotations (including Hadamard) and CNOT operations. In this context, $\hat{\mathcal{C}}^{i,j}_{SO-SO(Mo-Mo)}$ represents SO-SO (Mo-Mo) CNOT gate between $i-th$ cell and $j-th$ Cell, and $\hat{\mathcal{C}}^{j,d}_{SO-Mo}$ represents SO-Mo CNOT gate in $j-th$ cell.

More precisely, for Eq. (28), generation entangled state $|\psi\rangle_{\text{hyper}}$ only required quantum gates sets belong to single DoF gates. To schedule this circuit for generating $|\psi\rangle_{\text{hyper}}$, two individual sets of quantum operation sequences are used for preparing $|GHZ\rangle_o$ in site-qubit-chain and $|GHZ\rangle_m$ within Mo-qubit-chain, respectively. Because the quantum operations on these two DoFs affect each other, the entangled states of qubits encoded in the two different DoFs $|GHZ\rangle_o$ and $|GHZ\rangle_m$ needs to be completed separately in different time at different time periods. As shown in Fig. 9(b), we first complete the preparation of entangled states at the SO DoF via performing a total of $n+1$ quantum gate operations (one $\hat{\mathcal{H}}^{j}_{SO}$ and $n$ $\hat{\mathcal{C}}^{i,j}_{SO-SO}$), and the key steps are as follows: First, a single qubit gate operation $\hat{\mathcal{H}}^{k}_{SO}$ was applied to the atoms trapped in the middle position $k = n/2$ ($n$ is even) or $k = (n+1)/2$ ($n$ is odd), and the system is evolved from the initial state Eq. (30) to:

$$|\psi\rangle_o^k = \frac{1}{\sqrt{2}}(|0\rangle_o^k + |1\rangle_o^k). \tag{31}$$

Then, a SO-SO CNOT gate $\hat{\mathcal{C}}^{k,k+1}_{SO}$ entangled the two atoms in the middle cell, and the corresponding state could be written as:

$$|GHZ\rangle_o^{k,k+1} = \frac{1}{\sqrt{2}}(|0,0\rangle_o^{k,k+1} + |1,1\rangle_o^{k,k+1}). \tag{32}$$

Next, under the combined action of these two quantum gates $\hat{\mathcal{C}}^{k,k-1}_{SO}$ and $\hat{\mathcal{C}}^{k+1,k+2}_{SO}$, the corresponding state evolved to a 4-qubits GHZ state:

$$|GHZ\rangle_o^{k-1,k,k+1,k+2} = \frac{1}{\sqrt{2}}(|0,0,0,0\rangle_o^{k-1,k,k+1,k+2} + |1,1,1,1\rangle_o^{k-1,k,k+1,k+2}). \tag{33}$$

On this basis, under the induction of a series of SO-SO CNOT gates, the region of GHZ entanglement is gradually extended from the middle region to the whole SO-qubits-chain and evolved to a n-qubits GHZ state $|GHZ\rangle_o$. Similarly, we repeat this operation array in Mo-qubits-chain and could construct a n-qubits GHZ state $|GHZ\rangle_m$. Meanwhile, the quantum state of the whole ladder-like system is $|\psi\rangle_{\text{hyper}}$. In the process of performing quantum circuits for the entangled state $|\psi\rangle_{\text{hyper}}$, we need to perform $2(n+1)$ quantum gate operations, and the corresponding circuit depth [46] results after decomposition is $n+2$ ($n$ is even) or $n+3$ ($n$ is odd).

Another key application is generating multi-qubit hyper-hybrid entangled states, such as $|\psi\rangle_{\text{hyper-hybrid}}$, which are specifically designed for generating the max entanglement using this two-DoF ladder-like device, as shown in Fig. 9(c). Starting with the initial state Eq. (30), the construction of $2n$ qubits GHZ state $|\psi\rangle_{\text{hyper-hybrid}}$ is incorporated with two elementary steps, including the preparation of $|GHZ\rangle_o$ and quantum manipulation across different DoFs. For the preparation of $n$ qubits GHZ state among $n$ different atoms encoded on SO DoF $|GHZ\rangle_o$, which is in the same way as the previously introduced method. Benefiting from the advantages of this system in parallel operations, we could based on the GHZ state in SO-qubit-chain simultaneously perform $n$ sets of $\hat{C}^{j,d}_{SO-Mo}$ for all atoms and obtain a global hyper-hybrid-GHZ state $|\psi\rangle_{\text{hyper-hybrid}}$. The hyper-hybrid-GHZ state $|\psi\rangle_{\text{hyper-hybrid}}$ is a highly entangled quantum state, in addition to SO-SO entangled and Mo-Mo entangled, different DoFs, i.e., SO and Mo DoF also intricately entangled with each other. The optimal quantum circuit for the entangled state $|\psi\rangle_{\text{hyper-hybrid}}$ can be decomposed into $2n+1$ quantum gates operations and the corresponding circuit depth results after decomposition is $n/2+2$ ($n$ is even) or $(n+1)/2+2$ ($n$ is odd).

## 6 Discussion on the experimental feasibility

The high-dimensional quantum computation scheme proposed in this work can be implemented with various alkali (earth) atoms, such as the $^{87}Rb$ and $^{87(88)}Sr$ atoms. For instance, the state-dependent storage and shuttle tweezers are readily implemented for $^{87}Rb$ atoms in the $5^2S_{1/2}$ manifold [47], and $^{87(88)}Sr$ atom in the $^1S_0$ and $^3P_0$ manifolds [26, 48–50]. Moreover, the Mo state manipulation and the motional-dependent hopping between tweezers of $^{87}Rb$ atoms have been experimentally demonstrated [5]. The erasure cooling scheme to prepare tweezer-trapped atoms in the motional ground state has been proposed for both $^{87}Rb$ and $^{87(88)}Sr$ atoms, and experimentally verified for $^{88}Sr$ atoms [27]. These developments guarantee the implementation of the ladder-shaped tweezer array with the additional shuttle tweezers, and the initial state preparations in the platform.

The LTA scheme suffers from imperfections in the realistic setup and operations, which can be categorized into the leakage beyond the computational basis, the static inhomogeneity of the tweezer arrays and the temporal effects, such as the long-term drift and the short-term noise of the laser systems. Taking the Mo-maintained spin rotation for instance, our numerical simulation shown in Fig. 7 has indicated that, the leakage to higher Mo states beyond the computational basis of $\{|s\rangle_m, |p\rangle_m\}$ would indeed lead to imperfection of the operation, while the infidelity caused by the leakage can be well suppressed by the energetical detuning between different Mo states, with the total fidelity reaching > 99%. Besides the global shot-to-shot fluctuations in trapping frequency, the inhomogeneity of the arrays refers to the difference in the trapping potential between different storage tweezers, as well as between the storage and shuttle tweezers. For one thing, it has been suggested [26, 27] that the dephasing introduced by the inhomogeneity between storage tweezers can be suppressed by the motional echo technique, which can be directly adapted to the LTA scheme. For another, the inhomogeneity-induced energy detuning of the Mo states between the storage and shuttle tweezers can be suppressed by the multi-chromatic synchronization schemes proposed in this work, given that the energy detuning is static and can be measured before the temporal modulation operations. It is also noticeable that the homogeneity control of the tweezer arrays has been experimentally improving, and the large-size array of uniform tweezers has been experimentally implemented [13]. The temporal imperfections determine the coherence and life times of the qubit states, and one can shed a light to the feasibility with respect to the temporal imperfections by comparing the operation time with the coherence time of the qubit states. Taking the motional qubit states for instance, which are more sensitive to the temporal imperfections, the Mo-related operation time according to the numerical simulation is on the order of 10 ms. The coherence time of the Mo states in the atomic tweezer array can reach 100 ms in experiments [27], which provides a support to the feasibility of the proposed LTA scheme.

The finite temperature would affect the coherence of the atom in the superposition states between different Mo or SO states. The deep cooling in the initial state preparation stage can well suppress this effect, and the Raman sideband cooling [5] and the erasure correction cooling [27] have been experimentally implemented for cooling the tweezer atoms to the ground Mo state, which is suitable for the LTA setup. Another error source is the heating caused by operations, e.g. the Raman process, and tweezer position manipulation. The atom heating resulting from tweezer position manipulation, including tweezer shaking and moving, has been taken into account in our first-principles numerical simulation, which indicates that the heating can be well

controlled with stable laser setups. The heating effect during the Raman process is small enough for our spin rotation process to be neglected, since our two-photon amplitude is far less than the normal two-photon Raman process to compatible Mo states.

## 7 Summary

In this work, we have introduced the high-dimensional universal quantum computation scheme in a ladder-shaped atomic tweezer array. The key strategy of the scheme is integrating different degrees of freedom to extend the single-atom computational basis to high dimensions and enable each atom to carry multiple qubits. The Mo and SO DoF are considered in this work to contribute to the computation basis, which doubles the quantum information capacity of a single atom. We have demonstrated the feasibility of the high-dimensional quantum computation through the integration of different DoFs in the LTA setup, with the concrete design of the quantum gates for the universal quantum computation.

The current work mainly focuses on the suppression of the inter-DoF crosstalk between qubits encoded into different DoFs, and a unified strategy composed of detuning engineering and the multi-chromatic synchronized Hamiltonian modulation is introduced to suppress such inter-DoF crosstalk. The experimental feasibility is also briefly discussed. The LTA scheme can be further improved by exploring the optimal control to simplify the operation elements and improve the fidelity. Moreover, this scheme can be further generalized to involve more degrees of freedom to enlarge the computational basis, such as the spin and the Mo DoF in different directions.

## Appendix A: Arbitrary single-qubit rotation operations

Here we introduce arbitrary single-qubit rotation operations in detail for various DoFs, including spin, Mo- and SO-, which provide elements for quantum gates fabrication.

### A.1 Spin arbitrary single-qubit operations

Two-photon Raman lasers can be utilized to arbitrarily transform spin states as we need, which provides a foundation for the spin arbitrary single-qubit operations. The two-photon Raman Hamiltonian have:

$$\begin{aligned}
\hat{H}_{Ra} &= -\frac{\hbar^2\vec{\nabla}^2}{2m} + \hat{V}_{Spin}(\vec{r}) + \sum_{\sigma=\downarrow,\uparrow,e} \varepsilon_\sigma |\sigma\rangle_s\langle\sigma| + \hbar\hat{\Omega}^{\alpha}_{Ra}(\vec{r}),\\
\hat{V}_{Spin}(\vec{r}) &= \hat{V}_{twz}[V_{sg},\vec{R}_1](\vec{r}) \otimes |\downarrow\rangle_s\langle\downarrow|\\
&\quad + \hat{V}_{twz}[V_{sh},\vec{R}_1](\vec{r}) \otimes |\uparrow\rangle_s\langle\uparrow|,\\
\hat{\Omega}^{\alpha}_{Ra}(\vec{r}) &= \tilde{\Omega}_{\alpha,1} f_{Ra}[\vec{R}_1,\sqrt{2}\vec{w}_{Ra}](\vec{r})\\
&\quad \times cos(\omega_{\alpha,1}t+\varphi_{\alpha,1})|\downarrow\rangle_s\langle e|\\
&\quad + \tilde{\Omega}_{\alpha,2} f_{Ra}[\vec{R}_1,\sqrt{2}\vec{w}_{Ra}](\vec{r})\\
&\quad \times cos(\omega_{\alpha,2}t+\varphi_{\alpha,2})|\uparrow\rangle_s\langle e| + h.c.,\\
f_{Ra}[\vec{R}_1,\vec{w}](\vec{r}) &= e^{-2(x-x_1)^2/w_x^2-2(y-y_1)^2/w_y^2},
\end{aligned} \tag{A.1}$$

where $\vec{w}_{Ra} = (w_x^{Ra}, w_y^{Ra})$, $\vec{R}_1 = (x_1, y_1)$, $\tilde{\Omega}_{\alpha,j}$, $\omega_{\alpha,j}$ and $\varphi_{\alpha,j}$ are the waist width, the equilibrium position, the peak amplitude, the frequency and the phase of the Raman laser denoting by $\alpha = s, p$ and $j = 1, 2$, $\varepsilon_\sigma$ denotes the energy of the internal state $|\sigma\rangle_s$, $e$ denotes excited states $|e\rangle_s$, $\omega_{\alpha,j}$ is the laser frequency and $\varphi_{\alpha,j}$ is laser phase. We set $\tilde{\Omega}_{\alpha,1} = \tilde{\Omega}_{\alpha,2}$, the effective two-photon Raman Hamiltonian thus have:

$$\begin{aligned}
\hat{H}^{eff}_{Ra} &= -\frac{\hbar^2\vec{\nabla}^2}{2m} + \hat{V}_{Spin}(\vec{r}) + \hbar\hat{\Omega}^{\alpha}_{eff}(\vec{r}),\\
\hat{\Omega}^{\alpha}_{eff}(\vec{r}) &= \tilde{\Omega}_\alpha f_{Ra}[\vec{R}_1,\vec{w}_{Ra}](\vec{r}) e^{i(\omega_\alpha t+\varphi_\alpha)}(|\downarrow\rangle_s\langle\uparrow| + h.c.)\\
&\quad + \tilde{\Omega}_\alpha f_{Ra}[\vec{R}_1,\vec{w}_{Ra}](\vec{r})(|\downarrow\rangle_s\langle\downarrow| + |\uparrow\rangle_s\langle\uparrow|),
\end{aligned} \tag{A.2}$$

of which $\tilde{\Omega}_\alpha = \frac{\tilde{\Omega}_{\alpha,1}\tilde{\Omega}_{\alpha,2}}{4(\omega_\downarrow-\omega_e)}$, $\omega_\alpha = \omega_{\alpha,1} - \omega_{\alpha,2} - (\varepsilon_\downarrow - \varepsilon_\uparrow)$ and $\varphi_\alpha = \varphi_{\alpha,1} - \varphi_{\alpha,2}$ denotes the effective amplitude, the effective frequency, and the biased phase of the TPR transition.

We can acquire reduced Hamiltonian for the basis states $\{|\alpha\rangle_m|\uparrow\rangle_s, |\alpha\rangle_m|\downarrow\rangle_s\}$

$$\hat{H}_{spin} = \begin{bmatrix} \epsilon_{\alpha,sh} + (\varepsilon_\downarrow - \varepsilon_\uparrow) & \hbar\frac{\Omega_\alpha}{2}e^{-i(\omega_\alpha t+\varphi_\alpha)} \\ \hbar\frac{\Omega_\alpha}{2}e^{i(\omega_\alpha t+\varphi_\alpha)} & \epsilon_{\alpha,sg} \end{bmatrix}, \tag{A.3}$$

where the tweezer energy $\epsilon_{\alpha,sg(sh)} = {}_m\langle\alpha|_s\langle\downarrow(\uparrow)|[-\frac{\hbar^2\vec{\nabla}^2}{2m} + \hat{V}_{SF}(\vec{r}) + \hbar\tilde{\Omega}_\alpha f_{Ra}[\vec{R}_0,\vec{w}_{Ra}](\vec{r})]|\downarrow(\uparrow)\rangle_s|\alpha\rangle_m$, and the amplitude $\frac{\Omega_\alpha}{2} = {}_m\langle\alpha|\tilde{\Omega}_\alpha f_{Ra}[\vec{R}_0,\vec{w}_{Ra}](\vec{r})|\alpha\rangle_m$ is the reduced two-photon Rabi frequency of the state $|\alpha\rangle_m|\downarrow(\uparrow)\rangle_s$. Then we perform a rotating wave approximation, giving:

$$\hat{H}^{rwa}_{spin}/\hbar = \begin{bmatrix} \frac{\delta_\alpha}{2} & \frac{\Omega_\alpha}{2}e^{-i\varphi_\alpha} \\ \frac{\Omega_\alpha}{2}e^{i\varphi_\alpha} & -\frac{\delta_\alpha}{2} \end{bmatrix}, \tag{A.4}$$

where detuning $\delta_\alpha = (\epsilon_{\alpha,sh} - \epsilon_{\alpha,sg})/\hbar - \omega_\alpha + (\varepsilon_\downarrow - \varepsilon_\uparrow)/\hbar$. When evolving a time $t = T_\alpha$, its evolution operator has:

$$\begin{aligned}&\hat{O}_{spin}[\theta,\varphi,\phi]\\&= e^{-i\phi/2}\\&\times\begin{bmatrix} cos(\theta)\frac{1-e^{i\phi}}{2}+\frac{1+e^{i\phi}}{2} & -sin(\theta)e^{-i\varphi}\frac{e^{i\phi}-1}{2}\\ -sin(\theta)e^{i\varphi}\frac{e^{i\phi}-1}{2} & -cos(\theta)\frac{1-e^{i\phi}}{2}+\frac{1+e^{i\phi}}{2}\end{bmatrix},\end{aligned} \tag{A.5}$$

where $cos(\theta) = \frac{\delta_\alpha}{\sqrt{\delta_\alpha^2+\Omega_\alpha^2}}$, $sin(\theta) = \frac{\Omega_\alpha}{\sqrt{\delta_\alpha^2+\Omega_\alpha^2}}$, $\varphi = \varphi_\alpha$ and $\phi = T_\alpha\sqrt{\delta_\alpha^2+\Omega_\alpha^2}$. Then an arbitrary rotation gate can be constructed as follows:

$$\begin{aligned}\hat{R}^\alpha_{spin}[\theta,\varphi] &= \hat{O}_{spin}[\theta,\varphi,\pi]\\ &= -i\begin{bmatrix} cos(\theta) & sin(\theta)e^{-i\varphi}\\ sin(\theta)e^{i\varphi} & -cos(\theta)\end{bmatrix}.\end{aligned} \tag{A.6}$$

The $(-i)$ term as a global phase can be neglected. Other gates can be derived from it, such as Pauli-X, Hadamard, phase, and $\pi/8$ gates, shown as below:

$$\begin{aligned}\hat{X}^\alpha_{spin} &= \hat{R}^\alpha_{spin}[\frac{\pi}{2},0] = \begin{bmatrix}0&1\\1&0\end{bmatrix},\\ \hat{H}^\alpha_{spin} &= \hat{R}^\alpha_{spin}[\frac{\pi}{4},0] = \frac{1}{\sqrt{2}}\begin{bmatrix}1&1\\1&-1\end{bmatrix},\\ \hat{S}^\alpha_{spin} &= \hat{R}^\alpha_{spin}[\frac{\pi}{2},-\frac{\pi}{4}]*\hat{R}^\alpha_{spin}[\frac{\pi}{2},0] = \begin{bmatrix}1&0\\0&i\end{bmatrix},\\ \hat{T}^\alpha_{spin} &= \hat{R}^\alpha_{spin}[\frac{\pi}{2},-\frac{\pi}{8}]*\hat{R}^\alpha_{spin}[\frac{\pi}{2},0] = \begin{bmatrix}1&0\\0&e^{i\frac{\pi}{4}}\end{bmatrix},\end{aligned} \tag{A.7}$$

where the global phases are neglected. Combining a two-qubit CNOT gate and a single-qubit arbitrary rotation gate, we can acquire a universal quantum gate set to approximate any unitary operation to arbitrary accuracy.

### A.2 Mo-dependent hopping arbitrary single-qubit operations

Considering two SO states which separately occupy two tweezers located in $\vec{R}_1$ and $\vec{R}_2$, an additional shaking potential with cosine periodic modulation $\hat{\Omega}_{shk}(t) = A_{\alpha_1-\alpha_2}\times cos(\omega_{\alpha_1-\alpha_2}t+\varphi_{\alpha_1-\alpha_2})V_{pot}(\vec{r})$ is performed between target tweezers to resonantly couple the two SO states. For a basis $\{|\vec{R}_1\rangle_o|\alpha_1\rangle_m, |\vec{R}_2\rangle_o|\alpha_2\rangle_m\}$, Hamiltonian have:

$$\hat{H}_{SO} = \begin{bmatrix}\epsilon_{\vec{R}_1,\alpha_1} & \hbar\Omega_{\alpha_1-\alpha_2}cos(\omega_{\alpha_1-\alpha_2}t+\varphi_{\alpha_1-\alpha_2})\\ \hbar\Omega_{\alpha_1-\alpha_2}cos(\omega_{\alpha_1-\alpha_2}t+\varphi_{\alpha_1-\alpha_2}) & \epsilon_{\vec{R}_2,\alpha_2}\end{bmatrix}, \tag{A.8}$$

where $\Omega_{\alpha_1-\alpha_2} = A_{\alpha_1-\alpha_2 m}\langle\alpha_1|_o\langle\vec{R}_1|V_{pot}(\vec{r})|\vec{R}_2\rangle_o|\alpha_2\rangle_m/\hbar$ is the Rabi frequency between the two basis states $|\vec{R}_1\rangle_o|\alpha_1\rangle_m$ and $|\vec{R}_2\rangle_o|\alpha_2\rangle_m$, and $\epsilon_{\vec{R},\vec{\alpha}}$ is the energy of the state $|\vec{R}\rangle_o|\vec{\alpha}\rangle_m$ with $\alpha_{1(2)} = s/p$ denotes correspond Mo state. Then we perform a rotating wave approximation, giving:

$$\hat{H}^{rwa}_{SO}/\hbar = \begin{bmatrix}\frac{\delta_{\alpha_1-\alpha_2}}{2} & \frac{\Omega_{\alpha_1-\alpha_2}}{2}e^{-i\varphi_{\alpha_1-\alpha_2}}\\ \frac{\Omega_{\alpha_1-\alpha_2}}{2}e^{i\varphi_{\alpha_1-\alpha_2}} & -\frac{\delta_{\alpha_1-\alpha_2}}{2}\end{bmatrix}, \tag{A.9}$$

where detuning $\delta_{\alpha_1-\alpha_2} = (\epsilon_{\vec{R}_1,\alpha_1} - \epsilon_{\vec{R}_2,\alpha_2})/\hbar - \omega_{\alpha_1-\alpha_2}$. We can get the evolution operator and rotation gate evolving a time $t = T_{\alpha_1-\alpha_2}$ as Appendix A.1, which have:

$$\begin{aligned}&\hat{O}_{SO}[\theta,\varphi,\phi]\\&= e^{-i\phi/2}\\&\times\begin{bmatrix} cos(\theta)\frac{1-e^{i\phi}}{2}+\frac{1+e^{i\phi}}{2} & -sin(\theta)e^{-i\varphi}\frac{e^{i\phi}-1}{2}\\ -sin(\theta)e^{i\varphi}\frac{e^{i\phi}-1}{2} & -cos(\theta)\frac{1-e^{i\phi}}{2}+\frac{1+e^{i\phi}}{2}\end{bmatrix},\\&\hat{R}^{\alpha_1\to\alpha_2}_{SO}[\theta,\varphi](\vec{R}_1\to\vec{R}_2)\\&= \hat{O}_{SO}[\theta,\varphi,\pi] = -i\begin{bmatrix} cos(\theta) & sin(\theta)e^{-i\varphi}\\ sin(\theta)e^{i\varphi} & -cos(\theta)\end{bmatrix},\end{aligned} \tag{A.10}$$

where $cos(\theta) = \frac{\delta_{\alpha_1-\alpha_2}}{\sqrt{\delta^2_{\alpha_1-\alpha_2}+\Omega^2_{\alpha_1-\alpha_2}}}$, $sin(\theta) = \frac{\Omega_{\alpha_1-\alpha_2}}{\sqrt{\delta^2_{\alpha_1-\alpha_2}+\Omega^2_{\alpha_1-\alpha_2}}}$, $\varphi = \varphi_{\alpha_1-\alpha_2}$ and $\phi = T_{\alpha_1-\alpha_2}\sqrt{\delta^2_{\alpha_1-\alpha_2}+\Omega^2_{\alpha_1-\alpha_2}}$.

### A.3 Mo arbitrary single-qubit operations

For a shaking tweezer given as Eq. 11, we can derive its reduced Hamiltonian for the basis states $\{|s\rangle_m, |p\rangle_m\}$, shown as below:

$$\hat{H}_{Mo} = \begin{bmatrix}\epsilon_s & \hbar\Omega(t)\\ \hbar\Omega(t) & \epsilon_p\end{bmatrix}, \tag{A.11}$$

where $\epsilon_{s(p)}$ is the energy of the Mo state $|s(p)\rangle_m$ and the coupling strength $\Omega(t) = {}_m\langle s|\hat{V}_{Mo}(t)|p\rangle_m/\hbar$ with a sine periodic modulation, which can be approximated as:

$$\begin{aligned}\Omega(t) &= \Omega_{Mo}cos(\omega_{Mo}t+\varphi_{Mo})+\Omega_0,\\ \Omega_{Mo} &= \Omega^{max}_{Mo}-\Omega^{min}_{Mo},\\ \Omega_0 &= (\Omega^{max}_{Mo}+\Omega^{min}_{Mo})/2,\end{aligned} \tag{A.12}$$

where the maximum and minimum of the coupling strength for the modulation tweezer are separately $\Omega^{max}_{Mo} = {}_m\langle s|V_{twz}[V_{sg},(x_c,y_c)]|p\rangle_m$ and $\Omega^{max}_{Mo} = {}_m\langle s|V_{twz}[V_{sg},(x_c+\tilde{\Omega}_{Mo},y_c)]|p\rangle_m$, which correspond to the shaking tweezer moving to the positions $(x_c,y_c)$ and $(x_c+\tilde{\Omega}_{Mo},y_c)$. Then we perform an rotating wave approximation and $\Omega_0$ is neglected as high frequency term, giving:

$$\hat{H}^{rwa}_{Mo}/\hbar = \begin{bmatrix}\frac{\delta_{Mo}}{2} & \frac{\Omega_{Mo}}{2}e^{-i\varphi_{Mo}}\\ \frac{\Omega_{Mo}}{2}e^{i\varphi_{Mo}} & -\frac{\delta_{Mo}}{2}\end{bmatrix}, \tag{A.13}$$

where the detuning $\delta_{Mo} = (\varepsilon_s-\varepsilon_p)/\hbar - \omega_{Mo}$.

We can get the evolution operator and arbitrary rotation gate evolving a time $t = T_{Mo}$ as Appendix A.1 and A.2, which have:

$$\begin{aligned}&\hat{O}_{Mo}[\theta,\varphi,\phi]\\&= e^{-i\phi/2}\begin{bmatrix} cos(\theta)\frac{1-e^{i\phi}}{2}+\frac{1+e^{i\phi}}{2} & -sin(\theta)e^{-i\varphi}\frac{e^{i\phi}-1}{2}\\ -sin(\theta)e^{i\varphi}\frac{e^{i\phi}-1}{2} & -cos(\theta)\frac{1-e^{i\phi}}{2}+\frac{1+e^{i\phi}}{2}\end{bmatrix},\\&\hat{R}_{Mo}[\theta,\varphi]\\&= \hat{O}_{Mo}[\theta,\varphi,\pi] = -i\begin{bmatrix} cos(\theta) & sin(\theta)e^{-i\varphi}\\ sin(\theta)e^{i\varphi} & -cos(\theta)\end{bmatrix},\end{aligned} \tag{A.14}$$

where $cos(\theta) = \frac{\delta_{Mo}}{\sqrt{\delta_{Mo}^2+\Omega_{Mo}^2}}$, $sin(\theta) = \frac{\Omega_{Mo}}{\sqrt{\delta_{Mo}^2+\Omega_{Mo}^2}}$, $\varphi = \varphi_{Mo}$ and $\phi = T_{Mo}\sqrt{\delta_{Mo}^2+\Omega_{Mo}^2}$.

## Appendix B: Quantum gate operations

To realize universal quantum computation, a set of universal quantum gates is required, which includes SO- and Mo- single-qubit arbitrary rotation gates, SO-Mo, SO-SO, and Mo-Mo two-qubit CNOT gates. Here we introduce the state transformations for these gates in detail.

### B.1 SO single-qubit arbitrary rotation gate

There are two ways to realize the SO single-qubit arbitrary rotation gate, including Mo-maintained shuttling and Mo-dependent hopping, which can transform SO qubits with arbitrary rotations, which are equal for their Mo states.

For the $j$-th cell, the initial states are $|\vec{R}_{j,u}\rangle_o|\alpha(\vec{\theta}_m)\rangle_m|\downarrow\rangle_s$ and $|\vec{R}_{j,d}\rangle_o|\alpha(\vec{\theta}_m)\rangle_m|\downarrow\rangle_s$. We introduce the first SO single-qubit arbitrary rotation gate, when the Mo-maintained shuttling $\hat{X}_{MmS}(\vec{R}_{j,u}\rightarrow\vec{R}_{j,d})$ exerting on the initial state, the Mo-states are projected into the spin stats, which have:

$$\begin{aligned}&\hat{X}_{MmS}(\vec{R}_{j,u}\rightarrow\vec{R}_{j,d})\begin{bmatrix}|\vec{R}_{j,u}\rangle_o\\ |\vec{R}_{j,d}\rangle_o\end{bmatrix}|\alpha(\vec{\theta}_m)\rangle_m|\downarrow\rangle_s\\&= |\vec{R}_{j,d}\rangle_o|\alpha(\vec{\theta}_m)\rangle_m\begin{bmatrix}|\uparrow\rangle_s\\ |\downarrow\rangle_s\end{bmatrix},\end{aligned} \tag{B.1}$$

where $|\alpha(\vec{\theta}_m)\rangle_m = cos(\theta_m)|s\rangle_m + sin(\theta_m)e^{i\varphi_m}|p\rangle_m$, and $\vec{\theta}_m = (\theta_m,\varphi_m)$. After that arbitrary single-qubit spin rotation $\hat{R}_{MmSF}[\theta,\varphi](\vec{R}_{j,d})$ can prepare the desired spin states as we need, which have:

$$\begin{aligned}&\hat{R}_{MmSF}[\theta,\varphi](\vec{R}_{j,d})|\vec{R}_{j,d}\rangle_o|\alpha(\vec{\theta}_m)\rangle_m\begin{bmatrix}|\uparrow\rangle_s\\ |\downarrow\rangle_s\end{bmatrix}\\&= |\vec{R}_{j,d}\rangle_o|\alpha(\vec{\theta}_m)\rangle_m\begin{bmatrix}|\sigma(\vec{\theta})\rangle_s\\ |\tilde{\sigma}(\vec{\theta})\rangle_s\end{bmatrix},\end{aligned} \tag{B.2}$$

where $|\sigma(\vec{\theta})\rangle_s = cos(\theta)|\uparrow\rangle_s + sin(\theta)e^{i\varphi}|\downarrow\rangle_s$, $|\tilde{\sigma}(\vec{\theta})\rangle_s = -sin(\theta)e^{-i\varphi}|\uparrow\rangle_s + cos(\theta)|\downarrow\rangle_s$, and $\vec{\theta} = (\theta,\varphi)$. Finally an inverse operation of the $\hat{X}_{MmS}(\vec{R}_{j,u}\rightarrow\vec{R}_{j,d})$ is performed, the spin states are projected into the SO states, which have:

$$\begin{aligned}&\hat{X}_{MmS}(\vec{R}_{j,u}\rightarrow\vec{R}_{j,d})^{-1}|\vec{R}_{j,d}\rangle_o|\alpha(\vec{\theta}_m)\rangle_m\begin{bmatrix}|\sigma(\vec{\theta})\rangle_s\\ |\tilde{\sigma}(\vec{\theta})\rangle_s\end{bmatrix}\\&= \begin{bmatrix}|\vec{R}_j(\vec{\theta})\rangle_o\\ |\tilde{\vec{R}}_j(\vec{\theta})\rangle_o\end{bmatrix}|\alpha(\vec{\theta}_m)\rangle|\downarrow\rangle_s,\end{aligned} \tag{B.3}$$

where $|\vec{R}_j(\vec{\theta})\rangle_o = cos(\theta)|\vec{R}_{j,u}\rangle_o + sin(\theta)e^{i\varphi}|\vec{R}_{j,d}\rangle_o$ and $|\tilde{\vec{R}}_j(\vec{\theta})\rangle_o = -sin(\theta)e^{-i\varphi}|\vec{R}_{j,u}\rangle_o + cos(\theta)|\vec{R}_{j,d}\rangle_o$.

For the second SO single-qubit gate, $\hat{R}_{SO}[\theta,\varphi](\vec{R}_{j,u};\vec{R}_{j,d})$ is utilized to rotate SO states, which have:

$$\begin{aligned}&\hat{R}_{SO}[\theta,\varphi](\vec{R}_{j,u};\vec{R}_{j,d})\begin{bmatrix}|\vec{R}_{j,u}\rangle_o\\ |\vec{R}_{j,d}\rangle_o\end{bmatrix}|\alpha(\vec{\theta}_m)\rangle_m|\downarrow\rangle_s\\&= \begin{bmatrix}|\vec{R}_j(\vec{\theta})\rangle_o\\ |\tilde{\vec{R}}_j(\vec{\theta})\rangle_o\end{bmatrix}|\alpha(\vec{\theta}_m)\rangle|\downarrow\rangle_s.\end{aligned} \tag{B.4}$$

Thus two kinds of SO single-qubit arbitrary rotation gates can realize the same state transformations, shown as below:

$$\begin{aligned}&\hat{\mathcal{U}}_{SO}^{j}[\theta,\varphi]\begin{bmatrix}|\vec{R}_{j,u}\rangle_o\\ |\vec{R}_{j,d}\rangle_o\end{bmatrix}|\alpha(\vec{\theta}_m)\rangle_m|\downarrow\rangle_s\\&= \begin{bmatrix}|\vec{R}_j(\vec{\theta})\rangle_o\\ |\tilde{\vec{R}}_j(\vec{\theta})\rangle_o\end{bmatrix}|\alpha(\vec{\theta}_m)\rangle|\downarrow\rangle_s.\end{aligned} \tag{B.5}$$

### B.2 Mo single-qubit arbitary rotation gate

For the Mo single-qubit arbitrary rotation gate, we use periodic modulation of the tweezer positions to flip Mo states. The initial states are $|\vec{R}_j(\vec{\theta}_o)\rangle_o|s\rangle_m|\downarrow\rangle_s$ and $|\vec{R}_j(\vec{\theta}_o)\rangle_o|p\rangle_m|\downarrow\rangle_s$, then the Mo- single-qubit arbitrary gate have:

$$\begin{aligned}&\hat{\mathcal{U}}_{Mo}^{j}[\theta,\varphi]|\vec{R}_j(\vec{\theta}_o)\rangle_o\begin{bmatrix}|s\rangle_m\\ |p\rangle_m\end{bmatrix}|\downarrow\rangle_s =\\&\qquad |\vec{R}_j(\vec{\theta}_o)\rangle_o\begin{bmatrix}|\alpha(\vec{\theta})\rangle_m\\ |\tilde{\alpha}(\vec{\theta})\rangle_m\end{bmatrix}|\downarrow\rangle_s,\end{aligned} \tag{B.6}$$

where $|\tilde{\alpha}(\vec{\theta})\rangle_m = -sin(\theta)e^{-i\varphi}|s\rangle_m + cos(\theta)|p\rangle_m$.

### B.3 SO-Mo two-qubit CNOT gate

For the SO-Mo two-qubit CNOT gate, the site-resolved periodic modulation is performed to flip the Mo states of the target tweezer. For the initial states $|\vec{R}_j(\vec{\theta}_o)\rangle_o|s\rangle_m|\downarrow\rangle_s$ and $|\vec{R}_j(\vec{\theta}_o)\rangle_o|p\rangle_m|\downarrow\rangle_s$, we take the $\hat{\mathcal{C}}_{SO-Mo}^{j,d}$ as example,

which have:

$$\begin{aligned}&\hat{\mathcal{C}}^{j,d}_{SO-Mo}|\vec{R}_j(\vec{\theta}_o)\rangle_o\begin{bmatrix}|s\rangle_m\\|p\rangle_m\end{bmatrix}|\downarrow\rangle_s\\&=\begin{bmatrix}cos(\theta_o)|\vec{R}_{j,u}\rangle_o|s\rangle_m+sin(\theta_o)e^{i\varphi_o}|\vec{R}_{j,d}\rangle_o|p\rangle_m\\cos(\theta_o)|\vec{R}_{j,u}\rangle_o|p\rangle_m+sin(\theta_o)e^{i\varphi_o}|\vec{R}_{j,d}\rangle_o|s\rangle_m\end{bmatrix}|\downarrow\rangle_s,\end{aligned}\tag{B.7}$$

where $\vec{\theta}_o=(\theta_o,\varphi_o)$.

### B.4 SO-SO two-qubit CNOT gate

Similar to the SO single-qubit gate, there are also two kinds of methods to assemble the SO-SO two-qubit CNOT gate. For the first gate, the operator $\hat{U}^{j_1,j_2}_{dMmS}$ exert on the initial states $|\vec{R}_{j_1}(\vec{\theta}_o)\rangle_o|\alpha(\vec{\theta}_{1m})\rangle_m|\downarrow\rangle_s\otimes|\vec{R}_{j_2,u}\rangle_o|\alpha(\vec{\theta}_{2m})\rangle_m|\downarrow\rangle_s$ and $|\vec{R}_{j_1}(\vec{\theta}_o)\rangle_o|\alpha(\vec{\theta}_{1m})\rangle_m|\downarrow\rangle_s\otimes|\vec{R}_{j_2,d}\rangle_o|\alpha(\vec{\theta}_{2m})\rangle_m|\downarrow\rangle_s$, the atoms in control and target tweezers are transported in two shuttle tweezers which located closely in $\vec{R}_{j_1,d}$ and $\vec{R}_{j_1,\tilde{d}}$, shown as below:

$$\begin{aligned}&\hat{X}^{j_1,j_2}_{dMmS}|\vec{R}_{j_1}(\vec{\theta}_o)\rangle_o|\alpha(\vec{\theta}_{1m})\rangle_m|\downarrow\rangle_s\otimes\begin{bmatrix}|\vec{R}_{j_2,u}\rangle_o\\|\vec{R}_{j_2,d}\rangle_o\end{bmatrix}\\&|\alpha(\vec{\theta}_{2m})\rangle_m|\downarrow\rangle_s=|\vec{R}_{j_1,d}\rangle_o|\alpha(\vec{\theta}_{1m})\rangle_m|\sigma(\vec{\theta}_o)\rangle_s\\&\otimes\begin{bmatrix}|\vec{R}_{j_1,\tilde{d}}\rangle_o|\downarrow\rangle_s\\|\vec{R}_{j_2,d}\rangle_o|\uparrow\rangle_s\end{bmatrix}|\alpha(\vec{\theta}_{2m})\rangle_m,\end{aligned}\tag{B.8}$$

where $\vec{\theta}_{1m}=(\theta_{1m},\varphi_{1m})$ and $\vec{\theta}_{2m}=(\theta_{2m},\varphi_{2m})$. Then after $\hat{U}^{C}_{MmSF}(\vec{R}_{j_1,d};\vec{R}_{j_1,\tilde{d}})$ spin states are flipped or not depending on whether the control atoms occupy the shuttle tweezer around the target tweezer, and after that spin states are re-projected into the SO states, which have:

$$\begin{aligned}&\hat{X}^{j_1,j_2}_{dMmS}{}^{-1}*\hat{U}^{C}_{MmSF}|\vec{R}_{j_1,d}\rangle_o|\alpha(\vec{\theta}_{1m})\rangle_m|\sigma(\vec{\theta}_o)\rangle_s\\&\otimes\begin{bmatrix}|\vec{R}_{j_1,\tilde{d}}\rangle_o|\downarrow\rangle_s\\|\vec{R}_{j_2,d}\rangle_o|\uparrow\rangle_s\end{bmatrix}|\alpha(\vec{\theta}_{2m})\rangle_m\\&=\begin{bmatrix}|\vec{R}_{j_1}(\vec{\theta}_o)\rangle_o\otimes|\vec{R}_{j_2,u}\rangle_o\\|\vec{R}'_{j_1}(\vec{\theta}_o)\rangle_o\otimes|\vec{R}_{j_2,d}\rangle_o\end{bmatrix}|\alpha(\vec{\theta}_{1m})\rangle_m|\downarrow\rangle_s\otimes|\alpha(\vec{\theta}_{2m})\rangle_m|\downarrow\rangle_s,\end{aligned}\tag{B.9}$$

where $|\vec{R}'_{j_1}(\vec{\theta}_o)\rangle_o=cos(\theta_o)|\vec{R}_{j_1,d}\rangle_o+sin(\theta_o)e^{i\varphi_o}|\vec{R}_{j_1,u}\rangle_o$. Then the SO state of the $j_1$ cell is flipped only when the SO state of the $j_2$ cell occupies the down tweezer.

The second SO-SO two-qubit CNOT gate is introduced as below. Firstly the control tweezer is moved between the target tweezers, preparing for the controlled Mo-dependent hopping, which has:

$$\begin{aligned}&\hat{X}_{MmS}(\vec{R}_{j_2,d}\rightarrow\vec{R}_{j_1,\tilde{y_c}})|\vec{R}_{j_1}(\vec{\theta}_o)\rangle_o|\alpha(\vec{\theta}_{1m})\rangle_m|\downarrow\rangle_s\otimes\begin{bmatrix}|\vec{R}_{j_2,u}\rangle_o\\|\vec{R}_{j_2,d}\rangle_o\end{bmatrix}\\&|\alpha(\vec{\theta}_{2m})\rangle_m|\downarrow\rangle_s=|\vec{R}_{j_1}(\vec{\theta}_o)\rangle_o|\alpha(\vec{\theta}_{1m})\rangle_m|\downarrow\rangle_s\\&\otimes\begin{bmatrix}|\vec{R}_{j_1,\tilde{y}_c}\rangle_o\\|\vec{R}_{j_2,d}\rangle_o\end{bmatrix}|\alpha(\vec{\theta}_{2m})\rangle_m|\downarrow\rangle_s.\end{aligned}\tag{B.10}$$

Then $\hat{X}^{C;j_1,j_2}_{dMdH}$ swaps the SO states of $j_1$ cell when atom in $j_2$ cell occupy the down tweezer, after that $\hat{X}^{j_1}_{dMmS}{}^{-1}$ move tweezers return their initial positions, which have:

$$\begin{aligned}&\hat{X}_{MmS}(\vec{R}_{j_2,d}\rightarrow\vec{R}_{j_1,\tilde{y_c}})^{-1}*\hat{U}^{C;j_1,j_2}_{dMdH}|\vec{R}_{j_1,d}\rangle_o|\alpha(\vec{\theta}_{1m})\rangle_m|\sigma(\vec{\theta}_o)\rangle_s\\&\otimes\begin{bmatrix}|\vec{R}_{j_1,\tilde{d}}\rangle_o|\downarrow\rangle_s\\|\vec{R}_{j_2,d}\rangle_o|\uparrow\rangle_s\end{bmatrix}|\alpha(\vec{\theta}_{2m})\rangle_m=\\&\begin{bmatrix}|\vec{R}_{j_1}(\vec{\theta}_o)\rangle_o\otimes|\vec{R}_{j_2,u}\rangle_o\\|\vec{R}'_{j_1}(\vec{\theta}_o)\rangle_o\otimes|\vec{R}_{j_2,d}\rangle_o\end{bmatrix}|\alpha(\vec{\theta}_{1m})\rangle_m|\downarrow\rangle_s\otimes|\alpha(\vec{\theta}_{2m})\rangle_m|\downarrow\rangle_s.\end{aligned}\tag{B.11}$$

Thus two kinds of SO-SO two-qubit CNOT gates can realize the same state transformations, shown as below:

$$\begin{aligned}&\hat{\mathcal{C}}^{j_1,j_2}_{SO-SO}|\vec{R}_{j_1}(\vec{\theta}_o)\rangle_o|\alpha(\vec{\theta}_{1m})\rangle_m|\downarrow\rangle_s\\&\otimes\begin{bmatrix}|\vec{R}_{j_2,u}\rangle_o\\|\vec{R}_{j_2,d}\rangle_o\end{bmatrix}|\alpha(\vec{\theta}_{2m})\rangle_m|\downarrow\rangle_s=\\&\begin{bmatrix}|\vec{R}_{j_1}(\vec{\theta}_o)\rangle_o\otimes|\vec{R}_{j_2,u}\rangle_o\\|\vec{R}'_{j_1}(\vec{\theta}_o)\rangle_o\otimes|\vec{R}_{j_2,d}\rangle_o\end{bmatrix}|\alpha(\vec{\theta}_{1m})\rangle_m|\downarrow\rangle_s\otimes|\alpha(\vec{\theta}_{2m})\rangle_m|\downarrow\rangle_s.\end{aligned}\tag{B.12}$$

### B.5 Mo-Mo two-qubit CNOT gate

For the Mo-Mo two-qubit CNOT gate, controlled Mo rotation can flip the Mo states in $j_1$ cell when $j_2$ cell atoms occupy the p Mo state. The initial states are $|\vec{R}_{j_1}(\vec{\theta}_{1o})\rangle_o|\alpha(\vec{\theta}_m)\rangle_m|\downarrow\rangle_s\otimes|\vec{R}_{j_2}(\vec{\theta}_{2o})\rangle_o|s\rangle_m|\downarrow\rangle_s$ and $|\vec{R}_{j_1}(\vec{\theta}_{1o})\rangle_o|\alpha(\vec{\theta}_m)\rangle_m|\downarrow\rangle_s\otimes|\vec{R}_{j_2}(\vec{\theta}_{2o})\rangle_o|p\rangle_m|\downarrow\rangle_s$, the operator $\hat{U}^{u}_{dMdS}$ move the two shuttle tweezers' p Mo states into s states of the control tweezers and remain the s states in the storage tweezers:

$$\begin{aligned}&\hat{X}^{j_1,j_2;u}_{dMdS}|\vec{R}_{j_1}(\vec{\theta}_{1o})\rangle_o|\alpha(\vec{\theta}_m)\rangle_m|\downarrow\rangle_s\otimes|\vec{R}_{j_2}(\vec{\theta}_{2o})\rangle_o\\&\begin{bmatrix}|s\rangle_m\\|p\rangle_m\end{bmatrix}|\downarrow\rangle_s=|\vec{R}_{j_1}(\vec{\theta}_{1o})\rangle_o|\alpha(\vec{\theta}_m)\rangle_m|\downarrow\rangle_s\\&\otimes\begin{bmatrix}|\vec{R}_{j_2}(\vec{\theta}_{2o})\rangle_o|\downarrow\rangle_s\\|\vec{R}_{j_1}(\vec{\theta}_{2o})\rangle_o|\uparrow\rangle_s\end{bmatrix}|s\rangle_m,\end{aligned}\tag{B.13}$$

where $|\vec{R}_{\tilde{j_1}}(\vec{\theta}_{2o})\rangle_o=cos(\theta_{o,2})|\vec{R}_{j_1,\tilde{u}_1}\rangle_o+sin(\theta_{o,2})e^{i\varphi_{o,2}}|\vec{R}_{j_1,\tilde{u}_2}\rangle_o$, $\vec{\theta}_{1o}=(\theta_{1o},\varphi_{1o})$ and $\vec{\theta}_{2o}=(\theta_{2o},\varphi_{2o})$. Two control tweezers are moved around the target tweezers to perform controlled Mo rotation, as $\hat{U}^{C;j_1,j_2}_{dMF}$, and then the tweezers are moved to return their initial positions, which have:

$$\begin{aligned}&\hat{X}^{j_1,j_2;d}_{dMdS}{}^{-1}*\hat{U}^{C;j_1,j_2}_{dMF}|\vec{R}_{j_1}(\vec{\theta}_{1o})\rangle_o|\alpha(\vec{\theta}_m)\rangle_m|\downarrow\rangle_s\\&\otimes\begin{bmatrix}|\vec{R}_{j_2}(\vec{\theta}_{2o})\rangle_o|\downarrow\rangle_s\\|\vec{R}_{\tilde{j_1}}(\vec{\theta}_{2o})\rangle_o|\uparrow\rangle_s\end{bmatrix}|s\rangle_m=|\vec{R}_{j_1}(\vec{\theta}_{1o})\rangle_o|\downarrow\rangle_s\\&\otimes|\vec{R}_{j_2}(\vec{\theta}_{2o})\rangle_o|\downarrow\rangle_s\begin{bmatrix}|\alpha(\vec{\theta}_m)\rangle_m\otimes|s\rangle_m\\|\alpha'(\vec{\theta}_m)\rangle_m\otimes|p\rangle_m\end{bmatrix},\end{aligned}\tag{B.14}$$

where $|\alpha'(\vec{\theta}_m)\rangle_m=cos(\theta_m)|p\rangle_m+sin(\theta_m)e^{i\varphi_m}|s\rangle_m$.

Thus the Mo-Mo two-qubit CNOT gate has:

$$\begin{aligned}&\hat{\mathcal{C}}^{j_1,j_2}_{Mo-Mo}|\vec{R}_{j_1}(\vec{\theta}_{1o})\rangle_o|\alpha(\vec{\theta}_m)\rangle_m|\downarrow\rangle_s \otimes |\vec{R}_{j_2}(\vec{\theta}_{2o})\rangle_o\\ &\begin{bmatrix}|s\rangle_m\\ |p\rangle_m\end{bmatrix}|\downarrow\rangle_s = |\vec{R}_{j_1}(\vec{\theta}_{1o})\rangle_o|\downarrow\rangle_s\\ &\otimes|\vec{R}_{j_2}(\vec{\theta}_{2o})\rangle_o|\downarrow\rangle_s\begin{bmatrix}|\alpha(\vec{\theta}_m)\rangle_m\otimes|s\rangle_m\\ |\alpha'(\vec{\theta}_m)\rangle_m\otimes|p\rangle_m\end{bmatrix}.\end{aligned} \tag{B.15}$$

## Appendix C: Numerical method and settiings

The numerical simulations in 3.3 employ the ab-initio method Multi-Layer Multi-Configuration Time-Dependent Hartree method for arbitrary species (ML-MCTDHX) [31–33]. A key advantage of this method lies in the fact that the total wave function of atoms is expanded by the temporal optimization single-particle functions rather than fixed basis states, which enables the efficient response of the atoms' wavefunction to the temporal modulation of the Hamiltonian. The ML-MCTDHX expansion of the wavefunction of atoms living in the high-dimensional space spanned by the x-, y-DoF as well as the spin DoF is shown in Fig. 10, which exhibits a multi-layer structure. In the multi-layer expansion, the top node denotes the total wavefunction $|\Psi(t)\rangle$, which is expanded as:

$$|\Psi(t)\rangle = \sum_{\vec{n}} C_{\vec{n}}(t)|\vec{n}\rangle, \tag{C.1}$$

where the state $|\vec{n} = (n_1,\ldots,n_m)\rangle$ refers to the second-quantization representation of $N$ atoms occupying $m$ single-particle functions (SPFs), with $n_1+\cdots+n_m = N$ and $n_j$ the number of atoms in the $j$-th SPF. The SPFs in the second layer of Fig. 10 are further expanded with respect to the direct products of the basis states of the x-, y-DoF, and the spin DoF, as:

$$|\varphi_j(t)\rangle = \sum_{j_x,j_y,j_s}|\varphi_{x,j_x}(t)\rangle|\varphi_{y,j_y}(t)\rangle|\varphi_{s,j_s}(t)\rangle, \tag{C.2}$$

where $|\varphi_{\alpha,j_\alpha}(t)\rangle$ is the temporal optimized basis states for the $\alpha$-DoF, with $\alpha\in\{x,y,s\}$. $|\varphi_{\alpha,j_\alpha}(t)\rangle$ is further expanded by the primitive basis states of the corresponding DoF, as:

$$\begin{aligned}|\varphi_{x,j_x}(t)\rangle &= \sum_{x=1}^{n_x}\varphi_{j_x}(x)|x\rangle,\\ |\varphi_{y,j_y}(t)\rangle &= \sum_{y=1}^{n_y}\varphi_{j_y}(y)|y\rangle,\\ |\varphi_{s,j_s}(t)\rangle &= \sum_{s=1}^{n_s}\varphi_{j_s}(s)|s\rangle.\end{aligned} \tag{C.3}$$

The primitive basis states of the x- and y-DoF are chosen in the method as the discrete variable representations of the real space functions and those of the spin DoF are the spin states $\{|\uparrow\rangle_s,|\downarrow\rangle_s\}$. In the numerical simulations, we choose two Mo basis states along the x direction with $m_x = 2$ and two SO basis states along the y direction with $m_y = 2$, as well as $n_s = 2$ for the spin states. The total number of the SPFs is taken as $m = 8$ for the simulation, i.e. no truncation is applied to Eq. (C.2).

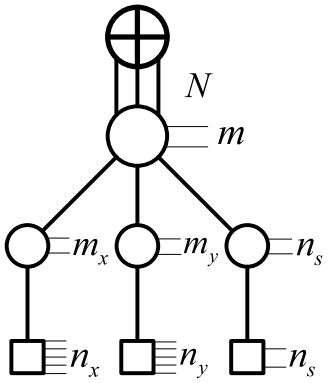


**Figure 10** The tree-diagram representation of wavefunction expansion used in the ML-MCTDHX simulation of this work. The tree diagram possesses multiple layers, and from bottom to up, the nodes on the first and second bottom layers denote the primitive and basis states for each DoF, respectively. The third layer counting from the bottom denotes the atom SPFs and the node on the top layer is the total wavefunction of the system

It is worth mentioning that the SPF for the single atom $|\varphi_j(t)\rangle$ and for each DoF $|\varphi_{x(y,s),j}(t)\rangle$ is temporally optimized according to the Dirac-Frenkel variational principle, and can well capture the wavefunction response to the time-dependent Hamiltonian, which is particularly suited to our simulation of the multi-chromatic modulations of the Hamiltonian. This is also manifested as the key difference between the ML-MCTDHX simulation with methods using fixed expansion, of which the basis states are fixed in time in spite of the temporal variation of the Hamiltonian.

Besides the wavefunction ansatz, we also introduce the Hamiltonian and the related parameters for the numerical simulations. The potential function of the tweezers is taken as Eq. (1) of the main text, and the waists for the storage (shuttle) tweezers are taken as $(w_x,w_y) = (1.5\mu m, 1\mu m)$. The depths of the storage and shuttle tweezers are taken as $V_{sg}/\hbar = -2\pi\times 40kHz$ and $V_{sh}/\hbar = -2\pi\times 20kHz$, respectively.

Mo-maintained spin rotation $\hat{X}_{MmSF}$ is realized by the TPR transition, which is modeled with the Hamiltonian as:

$$\hat{H} = -\frac{\hbar^2\vec{\nabla}^2}{2m} + \hat{V}_{Spin}(\vec{r}) + \sum_{\alpha=s,p}\hat{\Omega}^{\alpha}_{eff}(\vec{r}), \tag{C.4}$$

where the terms $\hat{V}_{Spin}(\vec{r})$ and $\hat{\Omega}^{\alpha}_{eff}(\vec{r})$ are expressed in Appendix A.1. In the above equation, the Raman lasers share

the same waist widths along the x and y direction as $w_x^{Ra} = w_x$ and $w_y^{Ra} = w_y$. Then the effective two-photon frequencies have $\omega_{s(p)} = (\epsilon_{s(p),sh} - \epsilon_{s(p),sg})/\hbar + (\varepsilon_\downarrow - \varepsilon_\uparrow)/\hbar = 2\pi \times 18.9376(18.0989)kHz$ to meet the resonant condition $\delta_{s(p)} = 0$. The effective two-photon amplitudes are taken as $\tilde{\Omega}_s = 2\pi \times 0.05kHz$ and $\tilde{\Omega}_p = r * \tilde{\Omega}_s$, for the s-s and p-p spin rotation, respectively. The Rabi frequency of the two Mo channel and consequently their ratio $r$ is directly calculated by substituting the exact spatial wavefunction of the Mo states and the spatial distribution of the Raman lasers to the integration of $r = \frac{m\langle s|f_{Ra}[\vec{R}_0,\vec{w}_{Ra}](\vec{r})|s\rangle_m}{m\langle p|f_{Ra}[\vec{R}_0,\vec{w}_{Ra}](\vec{r})|p\rangle_m}$, which leads to $r = 1.0646$ and the synchronized Rabi frequency $\Omega = \Omega_s = \Omega_p = 2\pi \times 0.093kHz$. Starting from the initial states $|\psi(t=0)\rangle = |\downarrow\rangle_s \otimes (|s\rangle_m + |p\rangle_m)/\sqrt{2}$, we acquire the evolving state $|\psi(t)\rangle$ under the above Hamiltonian in the Eq. (C.4), giving the basis-state probability $P_{|b\rangle}(t) = |\langle b|\psi(t)\rangle|^2$. Our simulation shows that, the fidelity $F_s = |_m\langle s|_s\langle\uparrow|\hat{X}_{MmSF}|\downarrow\rangle_s|s\rangle_m|^2 = 2P_{|\uparrow,s\rangle}(T_s)$ and $F_p = |_m\langle p|_s\langle\uparrow|\hat{X}_{MmSF}|\downarrow\rangle_s|p\rangle_m|^2 = 2P_{|\uparrow,p\rangle}(T_p)$ are both above 99.9% with evolution time $T_s = T_p = \frac{\pi}{\Omega} \approx 5.2ms$ and phase $\varphi = 0$, which can be further improved by optimizing parameters.

The Mo rotation is done with the temporal modulation of the storage tweezer, as

$$\hat{H} = -\frac{\hbar^2\vec{\nabla}^2}{2m} + \hat{V}_{Mo}, \tag{C.5}$$

where the term $\hat{V}_{Mo}$ is expressed in Eq. 11. The modulation amplitude is $\tilde{\Omega}_{Mo} = 0.002\mu m$, which contributing to a Rabi frequency $\Omega_{Mo} = 2\pi \times 0.0189kHz$, and modulation frequency $\omega_{Mo} = 2\pi \times 2.7198kHz$. Starting from the initial states $|\psi(t=0)\rangle = |s\rangle_m$, we acquire the evolving states $|\psi(t)\rangle$ under the above Hamiltonian in the Eq. (C.5). Our simulation demonstrates that, during a evolution of $T_{Mo} = \frac{\pi}{\Omega_{Mo}} \approx 26.7ms$ and phase $\varphi_{Mo} = 0$ of the $\hat{X}_{Mo}$, the fidelity $F = |_m\langle p|\hat{X}_{Mo}|s\rangle_m|^2 = |_m\langle p|\psi(T_{Mo})\rangle|^2$ is above 98%. Similarly, this fidelity can be improved by optimizing parameters.

The Mo-maintained transport element $\hat{T}_{MmT}$ is done with the following Hamiltonian term

$$\begin{aligned}\hat{H} &= -\frac{\hbar^2\vec{\nabla}^2}{2m} + \hat{V}_{move},\\ \hat{V}_{move} &= V_{twz}[V_{sh}, \vec{R}_c(t))](\vec{r})\,|\uparrow\rangle_s\langle\uparrow|,\end{aligned} \tag{C.6}$$

the distances from initial position $\vec{R}_c = (x_c, y_c)$ to target positions $\vec{R}^x_{tar} = (x_c + \Delta x, y_c)$ and $\vec{R}^y_{tar} = (x_c, y_c + \Delta y)$ are $\Delta x = \Delta y = 8\mu m$ with tweezer potential $20kHz$. Starting from the initial states $|\psi(t=0)\rangle = |\vec{R}_{ini}\rangle_o \otimes |p\rangle_m$, we acquire the evolving states $|\psi(t)\rangle = \psi(\vec{r},t)|\vec{r}\rangle$ under the above Hamiltonian in the Eq. (C.6), giving the one-body density $\rho(\vec{r},t) = |\psi(\vec{r},t)|^2$, in the simulation the basis state $|\vec{r}\rangle = |x\rangle \otimes |y\rangle$. The moving time $T$ is $5ms$ with fidelity $|_m\langle p|_o\langle\vec{R}^x_{tar}|\hat{T}_{MmT}(\vec{R}_c \to \vec{R}^x_{tar})|\vec{R}_{ini}\rangle_o|p\rangle_m|^2$ and $|_m\langle p|_o\langle\vec{R}^y_{tar}|\hat{T}_{MmT}(\vec{R}_c \to \vec{R}^y_{tar})|\vec{R}_{ini}\rangle_o|p\rangle_m|^2$ above 99% and 99.9%, respectively, which can be further improved by optimizing parameters and moving methods. The evolution time is simulated as $6ms$.

We also provide the comparison of different temporal functions of the moving trajectories of the tweezer, and consider the sinusoidal and linear function of:

$$\begin{aligned}\vec{R}^{sin}_c(t) &= \vec{R}_{ini} + (\vec{R}_{tar} - \vec{R}_{ini})\frac{sin(\frac{\pi t}{T} - \frac{\pi}{2}) + 1}{2},\\ \vec{R}^{str}_c(t) &= \vec{R}_{ini} + \frac{\vec{R}_{tar} - \vec{R}_{ini}}{T}t.\end{aligned} \tag{C.7}$$

Figure 11 presents the numerical simulation of the transport of the atom in the $|p\rangle_m$ state with the two temporal trajectories and the one-body density is plotted as a function of time, which can directly visualize the stability of the $|p\rangle_m$ state along the transport. From the numerical simulation, one can find that the fidelity of the $|p\rangle_m$ during the transport along the x-direction, i.e. $|_m\langle p|_o\langle\vec{R}^x_{tar}|\hat{T}_{MmT}(\vec{R}_c \to \vec{R}^x_{tar})|\vec{R}_{ini}\rangle_o|p\rangle_m|^2$ is above 99% with the temporal trajectory $\vec{R}^{sin}_c(t)$, while the same fidelity for the moving path with $\vec{R}^{str}_c(t)$ drops below 46%. And the fidelity of the $|p\rangle_m$ during the transport along y-direction i.e. $|_m\langle p|_o\langle\vec{R}^y_{tar}|\hat{T}_{MmT}(\vec{R}_c \to \vec{R}^y_{tar})|\vec{R}_{ini}\rangle_o|p\rangle_m|^2$ is above 99.9% with $\vec{R}^{sin}_c(t)$, and drops below 87% with $\vec{R}^{str}_c(t)$. The comparison indicates that the optimization can indeed improve the stability of the Mo states during trans-

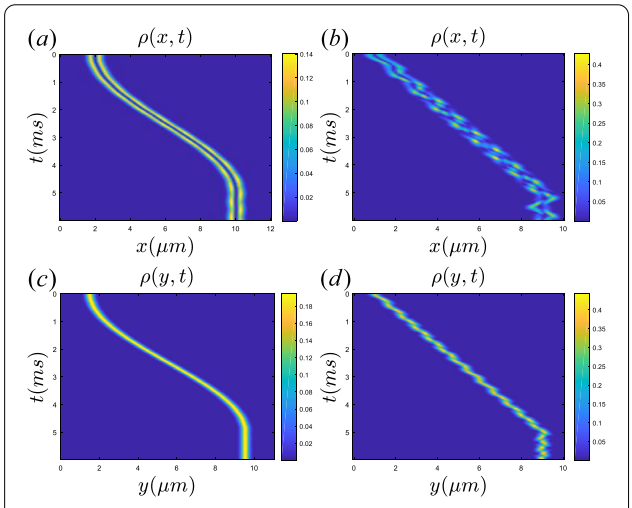


**Figure 11** The one-body density $\rho(x,t) = \sum_y \rho(\vec{r},t)$ along the x-axis for the Mo-state $|p\rangle_m$ in the moving tweezer with (a) $\vec{R}^{sin}_c(t)$ and (b) $\vec{R}^{str}_c(t)$ temporal trajectories. The one-body density $\rho(y,t) = \sum_x \rho(\vec{r},t)$ along the y axis for the Mo-state $|p\rangle_m$ with (c) $\vec{R}^{sin}_c(t)$ and (d) $\vec{R}^{str}_c(t)$ temporal trajectories

port, and the trajectories can be further optimized to increase the fidelity with a shorter transporting time.

**Author contributions**
ZKH, LC and XFX initialed the project and guided the whole investigation and manuscript writing. XD participated in tweezer array configuration design, and quantum gate design; and conducted quantum circuits for hyper- and hybrid entanglement. GP conducted tweezer array configuration design and quantum gate design. DX conducted the verification of the experimental feasibility of the designs. All authors contributed to the manuscript preparation and proofreading. All authors have read and approved the manuscript.

**Funding**
This work was supported by the Key Research and Development Program of China (Grants No.2022YFA1404102, No. 2022YFC3003802 and No. 2021YFB3900204), the Research Project of Hubei Education Department(Grants No. B2023077) and the Doctoral Scientific Research Foundation of Hubei University of Automotive Technology (Grants No. BK202432).

**Data availability**
All data underlying the results are available from the corresponding authors upon reasonable request.

## Declarations

**Consent for publication**
Not applicable.

**Competing interests**
Zhong-Kun Hu is an editorial board member for Quantum Frontiers and was not involved in the editorial review, or the decision to publish this article. All authors declare that there are no competing interests.

**Author details**
[1]MOE Key Laboratory of Fundamental Physical Quantities Measurement, Hubei Key Laboratory of Gravitation and Quantum Physics, PGMF, and School of Physics, Huazhong University of Science and Technology, Wuhan 430074, People's Republic of China. [2]Shiyan Key Laboratory of Quantum Information and Precision Optics, and School of Mathematics, Physics and Optoelectronic Engineering, Hubei University of Automotive Technology, Shiyan 442002, People's Republic of China. [3]Graduate School of China Academy of Engineering Physics, Beijing 100193, P.R. China.

Received: 22 October 2024 Revised: 31 January 2025
Accepted: 15 February 2025 Published online: 10 March 2025

**References**

1. A.M. Kaufman, B.J. Lester, C.M. Reynolds, M.L. Wall, M. Foss-Feig, K.R.A. Hazzard, A.M. Rey, C.A. Regal, Two-particle quantum interference in tunnel-coupled optical tweezers. Science **345**(6194), 306–309 (2014)
2. V. Bharti, S. Sugawa, M. Kunimi, V.S. Chauhan, T.P. Mahesh, M. Mizoguchi, T. Matsubara, T. Tomita, S. de Léséleuc, K. Ohmori, Strong spin-motion coupling in the ultrafast dynamics of Rydberg atoms. Phys. Rev. Lett. **133**(9), 093405 (2024)
3. H. Bernien, S. Schwartz, A. Keesling, H. Levine, A. Omran, H. Pichler, S. Choi, A.S. Zibrov, M. Endres, M. Greiner, V. Vuletić, M.D. Lukin, Probing many-body dynamics on a 51-atom quantum simulator. Nature **551**(7682), 579–584 (2017)
4. A. Browaeys, T. Lahaye, Many-body physics with individually controlled Rydberg atoms. Nat. Phys. **16**(2), 132–142 (2020)
5. M.O. Brown, S.R. Muleady, W.J. Dworschack, R.J. Lewis-Swan, A.M. Rey, O. Romero-Isart, C.A. Regal, Time-of-flight quantum tomography of an atom in an optical tweezer. Nat. Phys. **19**(4), 569–573 (2023)
6. E. Urban, T.A. Johnson, T. Henage, L. Isenhower, D.D. Yavuz, T.G. Walker, M. Saffman, Observation of Rydberg blockade between two atoms. Nat. Phys. **5**(2), 110–114 (2009)
7. T. Wilk, A. Gaëtan, C. Evellin, J. Wolters, Y. Miroshnychenko, P. Grangier, A. Browaeys, Entanglement of two individual neutral atoms using Rydberg blockade. Phys. Rev. Lett. **104**(1), 010502 (2010)
8. M. Saffman, Quantum computing with atomic qubits and Rydberg interactions: progress and challenges. J. Phys. B, At. Mol. Opt. Phys. **49**(20), 202001 (2016)
9. T.M. Graham, M. Kwon, B. Grinkemeyer, Z. Marra, X. Jiang, M.T. Lichtman, Y. Sun, M. Ebert, M. Saffman, Rydberg-mediated entanglement in a two-dimensional neutral atom qubit array. Phys. Rev. Lett. **123**(23), 230501 (2019)
10. Y. Wu, S. Kolkowitz, S. Puri, J.D. Thompson, Erasure conversion for fault-tolerant quantum computing in alkaline Earth Rydberg atom arrays. Nat. Commun. **13**(1), 4657 (2022)
11. B. Daniel, L. de Sylvain, L. Vincent, L. Thierry, B. Antoine, An atom-by-atom assembler of defect-free arbitrary two-dimensional atomic arrays. Science **354**(6315), 1021–1023 (2016)
12. C. Chen, G. Bornet, M. Bintz, G. Emperauger, L. Leclerc, V.S. Liu, P. Scholl, D. Barredo, J. Hauschild, S. Chatterjee, M. Schuler, A.M. Läuchli, M.P. Zaletel, T. Lahaye, N.Y. Yao, A. Browaeys, Continuous symmetry breaking in a two-dimensional Rydberg array. Nature **616**(7958), 691–695 (2023)
13. D. Bluvstein, S.J. Evered, A.A. Geim, S.H. Li, H. Zhou, T. Manovitz, S. Ebadi, M. Cain, M. Kalinowski, D. Hangleiter, A.J.P. Bonilla, N. Maskara, I. Cong, X. Gao, R.P. Sales, T. Karolyshyn, G. Semeghini, M. Gullans, M. Greiner, V. Vuletić, M.D. Lukin, Logical quantum processor based on reconfigurable atom arrays. Nature **626**(7997), 58–65 (2024)
14. D. Barredo, V. Lienhard, S. de Léséleuc, T. Lahaye, A. Browaeys, Synthetic three-dimensional atomic structures assembled atom by atom. Nature **561**(7721), 79–82 (2018)
15. A. Kumar, T.-Y. Wu, F. Giraldo, D.S. Weiss, Sorting ultracold atoms in a three-dimensional optical lattice in a realization of Maxwell's demon. Nature **561**(7721), 83–87 (2018)
16. H. Levine, A. Keesling, G. Semeghini, O. Ahmed, T.T. Wang, S. Ebadi, H. Bernien, M. Greiner, V. Vuletić, H. Pichler, L.D. Lukin, Parallel implementation of high-fidelity multiqubit gates with neutral atoms. Phys. Rev. Lett. **123**(17), 170503 (2019)
17. S.J. Evered, D. Bluvstein, M. Kalinowski, S. Ebadi, T. Manovitz, H. Zhou, S.H. Li, A.A. Geim, T.T. Wang, N. Maskara, H. Levine, G. Semeghini, M. Greiner, V. Vuletić, M.D. Lukin, High-fidelity parallel entangling gates on a neutral-atom quantum computer. Nature **622**(7982), 268–272 (2023)
18. S. Ebadi, T.T. Wang, H. Levine, A. Keesling, G. Semeghini, A. Omran, D. Bluvstein, R. Samajdar, H. Pichler, W.W. Ho, S. Choi, S. Sachdev, M. Greiner, V. Vuletić, M.D. Lukin, Quantum phases of matter on a 256-atom programmable quantum simulator. Nature **595**(7866), 227–232 (2021)
19. G. Semeghini, H. Levine, A. Keesling, S. Ebadi, T.T. Wang, D. Bluvstein, R. Verresen, H. Pichler, M. Kalinowski, R. Samajdar, A. Omran, S. Sachdev, A. Vishwanath, M. Greiner, V. Vuletić, M.D. Lukin, Probing topological spin liquids on a programmable quantum simulator. Science **374**, 1242–1247 (2021)
20. T.M. Graham, Y. Song, J. Scott, C. Poole, L. Phuttitarn, K. Jooya, P. Eichler, X. Jiang, A. Marra, B. Grinkemeyer, M. Kwon, M. Ebert, J. Cherek, M.T. Lichtman, M. Gillette, J. Gilbert, D. Bowman, T. Ballance, C. Campbell, E.D. Dahl, O. Crawford, N.S. Blunt, B. Rogers, T. Noel, M. Saffman, Multi-qubit entanglement and algorithms on a neutral-atom quantum computer. Nature **604**(7906), 457–462 (2022)
21. D. Bluvstein, H. Levine, G. Semeghini, T.T. Wang, S. Ebadi, M. Kalinowski, A. Keesling, N. Maskara, H. Pichler, M. Greiner, V. Vuletić, M.D. Lukin, A quantum processor based on coherent transport of entangled atom arrays. Nature **604**(7906), 451–456 (2022)
22. M. Saffman, Quantum computing with neutral atoms. Natl. Sci. Rev. **6**(1), 24–25 (2018)
23. A. Erhard, J.J. Wallman, L. Postler, M. Meth, R. Stricker, E.A. Martinez, P. Schindler, T. Monz, J. Emerson, R. Blatt, Characterizing large-scale quantum computers via cycle benchmarking. Nat. Commun. **10**(1), 5347 (2019)
24. F. Cesa, H. Pichler, Universal quantum computation in globally driven Rydberg atom arrays. Phys. Rev. Lett. **131**(17), 170601 (2023)
25. A.M. Kaufman, B.J. Lester, M. Foss-Feig, M.L. Wall, A.M. Rey, C.A. Regal, Entangling two transportable neutral atoms via local spin exchange. Nature **527**(7577), 208–211 (2015)
26. D. González-Cuadra, D. Bluvsteinc, M. Kalinowski, R. Kaubruegger, N. Maskara, P. Naldesi, T.V. Zache, A.M. Kaufman, M.D. Lukinc, H. Pichler, B. Vermersch, J. Ye, P. Zoller, Fermionic quantum processing with programmable neutral atom arrays. Proc. Natl. Acad. Sci. **120**(35), e2304294120 (2023)
27. A.L. Shaw, P. Scholl, R. Finkelstein, R.B. Tsai, J. Choi, M. Endres, Erasure-cooling, control, and hyper-entanglement of motion in optical tweezers (2024). arXiv:2311.15580v2

28. R. Ma, M.E. Tai, P.M. Preiss, W.S. Bakr, J. Simon, M. Greiner, Photon-assisted tunneling in a biased strongly correlated Bose gas. Phys. Rev. Lett. **107**(9), 095301 (2011)
29. Y.A. Chen, S. Nascimbène, M. Aidelsburger, M. Atala, S. Trotzky, I. Bloch, Controlling correlated tunneling and superexchange interactions with ac-driven optical lattices. Phys. Rev. Lett. **107**(21), 210405 (2021)
30. R. Gerritsma, A. Negretti, H. Doerk, Z. Idziaszek, T. Calarco, F. Schmidt-Kaler, Bosonic Josephson junction controlled by a single trapped ion. Phys. Rev. Lett. **109**(8), 080402 (2012)
31. S. Krönke, L. Cao, O. Vendrell, P. Schmelcher, Non-equilibrium quantum dynamics of ultra-cold atomic mixtures: the multi-layer multi-configuration time-dependent Hartree method for bosons. New J. Phys. **15**(6), 063018 (2013)
32. L. Cao, S. Krönke, O. Vendrell, P. Schmelcher, The multi-layer multi-configuration time-dependent Hartree method for bosons: theory, implementation, and applications. J. Chem. Phys. **139**(13), 134103 (2013)
33. L. Cao, V. Bolsinger, S.I. Mistakidis, G.M. Koutentakis, S. Krönke, J.M. Schurer, P. Schmelcher, A unified ab initio approach to the correlated quantum dynamics of ultracold fermionic and bosonic mixtures. J. Chem. Phys. **147**(4), 044106 (2017)
34. M.R. Lam, N. Peter, T. Groh, W. Alt, C. Robens, D. Meschede, A. Negretti, S. Montangero, T. Calarco, A. Alberti, Demonstration of quantum brachistochrones between distant states of an atom. Phys. Rev. X **11**(1), 011035 (2021)
35. Y. Li, M. Gessner, W. Li, A. Smerzi, Hyper- and hybrid nonlocality. Phys. Rev. Lett. **120**(5), 050404 (2018)
36. Y. Nam, Y. Su, D. Maslov, Approximate quantum Fourier transform with O(nlog(n)) T gates. npj Quantum Inf. **6**(1), 26 (2020)
37. V. Vorobyov, S. Zaiser, N. Abt, J. Meinel, D. Dasari, P. Neumann, J. Wrachtrup, Quantum Fourier transform for nanoscale quantum sensing. npj Quantum Inf. **7**(1), 124 (2021)
38. S. Backens, A. Shnirman, Y. Makhlin, Jordan–Wigner transformations for tree structures. Sci. Rep. **9**(1), 2598 (2019)
39. Z. Zhou, C. Liu, Z. Yan, Y. Chen, X-F. Zhang, Quantum dynamics of topological strings in a frustrated Ising antiferromagnet. npj Quantum Mater. **7**(1), 60 (2022)
40. C. Figgatt, D. Maslov, K.A. Landsman, N.M. Linke, S. Debnath, C. Monroe, Complete 3-qubit Grover search on a programmable quantum computer. Nat. Commun. **8**(1), 1918 (2017)
41. A. Al-Bayaty, M. Perkowski, A concept of controlling Grover diffusion operator: a new approach to solve arbitrary Boolean-based problems. Sci. Rep. **14**(1), 23570 (2024)
42. J. Yi, W. Ye, D. Gottesman, Z-W. Liu, Complexity and order in approximate quantum error-correcting codes. Nat. Phys. **20**(11), 1798–1803 (2024)
43. D.W. Leung, M.A. Nielsen, I.L. Chuang, Y. Yamamoto, Approximate quantum error correction can lead to better codes. Phys. Rev. A **56**(4), 2567–2573 (1997)
44. P. Hayden, S. Nezami, S. Popescu, G. Salton, Error correction of quantum reference frame information. PRX Quantum **2**(1), 010326 (2021)
45. S. Das, G. Paul, A. Banerji, Hyper-hybrid entanglement, indistinguishability, and two-particle entanglement swapping. Phys. Rev. A **102**(5), 052401 (2020)
46. A. Holmes, S. Johri, G.G. Guerreschi, J.S. Clarke, A.Y. Matsuura, Impact of qubit connectivity on quantum algorithm performance. Quantum Sci. Technol. **5**(2), 025009 (2020)
47. Z. Meng, L. Wang, W. Han, F. Liu, K. Wen, C. Gao, P. Wang, C. Chin, J. Zhang, Atomic Bose–Einstein condensate in twisted-bilayer optical lattices. Nature **615**(7951), 231–236 (2023)
48. A.J. Daley, M.M. Boyd, J. Ye, P. Zoller, Quantum computing with alkaline-Earth-metal atoms. Phys. Rev. Lett. **101**(17), 170504 (2008)
49. A. Cooper, J.P. Covey, I.S. Madjarov, S.G. Porsev, M.S. Safronova, M. Endres, Alkaline-Earth atoms in optical tweezers. Phys. Rev. X **8**(4), 041055 (2018)
50. A. Heinz, A.J. Park, N. Šantić, J. Trautmann, S.G. Porsev, M.S. Safronova, S. Blatt, State-dependent optical lattices for the strontium optical qubit. Phys. Rev. Lett. **124**(20), 203201 (2020)


## Publisher's Note